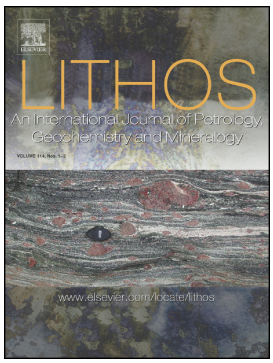

Suprasubduction-zone origin of the podiform chromitites of the Bir Tuluhah ophiolite, Saudi Arabia, during Neoproterozoic assembly of the Arabian Shield

Bassam A. Abuamarah, Paul D. Asimow, Mokhles K. Azer, Habes Ghrefat

PII: S0024-4937(20)30076-1

DOI: https://doi.org/10.1016/j.lithos.2020.105439

Reference: LITHOS 105439

To appear in: *LITHOS*

Received date: 10 January 2020

Revised date: 16 February 2020

Accepted date: 17 February 2020

Please cite this article as: B.A. Abuamarah, P.D. Asimow, M.K. Azer, et al., Suprasubduction-zone origin of the podiform chromitites of the Bir Tuluhah ophiolite, Saudi Arabia, during Neoproterozoic assembly of the Arabian Shield, *LITHOS*(2020), https://doi.org/10.1016/j.lithos.2020.105439

Suprasubduction-zone origin of the podiform chromitites of the Bir Tuluhah ophiolite, Saudi Arabia, during Neoproterozoic assembly of the Arabian Shield

Bassam A. Abuamarah[1], Paul D. Asimow[2], Mokhles K. Azer[3], Habes Ghrefat[1]

[1]Department of Geology and Geophysics, King Saud University, Riyadh 11451, Saudi Arabia

[2]Division of Geological & Planetary Sciences, California Institute of Technology, Pasadena CA 91125 USA

[3]Geological Sciences Department, National Research Centre, 12622-Dokki, Cairo, Egypt

Abstract

The ultramafic section of a dismembered ophiolite is exposed at Bir Tuluhah, in the north-central part of the Arabian Shield. It is penetratively serpentinized and locally carbonate-altered to talc-carbonate and quartz-carbonate rocks (listvenite) along shear zones and fault planes. Despite the high degree of mineral replacement, preserved mesh and bastite textures and fresh relics of primary Cr-spinel and olivine show that the protoliths were mainly harzburgite with minor dunite, with sparse massive chromitite bodies of various forms and sizes. Olivine inclusions in the chromitite lenses have higher forsterite content and NiO concentrations than fresh olivine relics in the host harzburgites and dunites, due to subsolidus re-equilibration. Cr-spinels in the chromitites have higher Cr# (0.74-0.82) than those hosted in dunite (0.72-0.76) or harzburgite (0.55-0.66). The scarce Cr-spinel crystals in harzburgite that have Cr# < 0.6 are interpreted to represent the population least affected by melt-rock interaction. The chromitite bodies are interpreted to have formed just below the contact between the oceanic crust and mantle sections (i.e., the petrologic Moho). The primary olivine (high Fo and Ni content) and Cr-spinel core compositions (high Cr# and low TiO_2 content) of the Bir Tuluhah serpentinized peridotite are typical of modern supra-subduction zone (SSZ) fore-arc peridotites and consistent with crystallization from boninitic magma. The multistage petrogenesis leading to the chromitite bodies begins with moderate to high degrees of melt extraction from the protoliths of the

serpentinized harzburgites, followed by reaction with melt compositions that evolved from tholeiite to boninite and left dunite residues. The massive Cr-rich chromitites in the Bir Tuluhah ophiolite are most probably the residues of such interaction between depleted harzburgite and ascending melts; mixtures of the reacted melts formed boninites, which became saturated with chrome-rich spinel and crystallized chromite pods before ascending past the Moho. We offer a novel thermodynamic model of this mixing and reaction process that quantifies the yield of Cr-spinel.

Keywords: Arabian Shield; Bir Tuluhah; Cr-rich chromitite; fore-arc; melt-rock reaction; supra-subduction zone.

1. Introduction

Neoproterozoic mafic-ultramafic complexes are widespread in the Arabian-Nubian Shield (ANS) and they preserve essential evidence of the geodynamic evolution of the orogenic belts within the Shield. The complexes can be divided into ophiolite belts and mafic–ultramafic intrusions (Stern et al., 2004; Ali et al., 2010; Johnson et al., 2004; Azer et al., 2017; Boskabadi et al., 2017). In the Arabian portion of the Shield, the ophiolites are mostly found along suture zones that extend roughly in a N-S direction (Fig. 1). Such ophiolites represent fragments of oceanic lithosphere that were tectonically obducted onto continental margins during collision between East and West Gondwana (e.g. Dilek and Ahmed, 2003; Kusky et al., 2003; Abuamarah, 2019 a,b; Gahlan et al., 2020). They are dismembered and have undergone multiple stages of metamorphism, deformation, and alteration (Nassief et al., 1984; Ahmed and Hariri, 2008; Abuamarah, 2019a, b; Gahlan et al., 2020). Their upper mantle sections expose highly serpentinized peridotite, mainly harzburgite with less abundant dunite. By contrast, the mafic-

ultramafic intrusions are fresh and unmetamorphosed having been emplaced in post-collisional settings (Moore and Al-Rehaili, 1989; Harbi, 2008); it has been suggested that some of these are concentrically zoned, Alaskan-type intrusions (e.g., Habtoor et al., 2016).

The Bir Tuluhah ophiolite belt is one of the most famous occurrences of ophiolite-hosted chromitite bodies in Saudi Arabia (Kattan, 1983; Al-Shanti and El-Mahdy, 1988; Habtoor et al., 2017). If its origin can be understood, it will serve as a key marker for the geodynamic evolution of the northeastern part of the Arabian Shield. However, previous interpretations of the Bir Tuluhah ultramafic section are wildly divergent (e.g. Delfour, 1977, Caby, 1982; Kattan, 1983; Le Metour et al., 1983; Pallister et al., 1987; Al-Shanti and El-Mahdy, 1988; Habtoor et al., 2017). Delfour (1977) defined the Bir Tuluhah ophiolite complex to include serpentinites, amphibolites, and some metabasalts and metasedimentary rocks. He considered this entire assemblage to be an island arc sequence deposited unconformably on the Hulayfah group. Caby (1982) concluded that the ultramafic rocks of Bir Tuluhah are not part of a classical ophiolite, but represent serpentinite diapirs emplaced along the sub-vertical Nabitah fault system. Le Metour et al. (1983) concluded that the protoliths of the Bir Tuluhah serpentinite were ultramafic cumulates representing subcontinental mantle and that the associated amphibolites are deep crustal metamorphic rocks. Pallister et al. (1987) described the Bir Tuluhah area as a west-dipping ophiolitic nappe obducted during the closure of an oceanic basin and rotated to high angles during formation of the Nabitah suture. Habtoor et al. (2017) studied high-Cr chromitites associated with the ultramafic rocks of Bir Tuluhah and assigned them to a supra-subduction zone (SSZ) setting without attempting to distinguish between fore-arc and back-arc environments.

This research is focused on the mantle section of the Neoproterozoic Bir Tuluhah ophiolite and associated chromitite bodies, in order to better understand their evolution during Neoproterozoic time. We present detailed field, petrographic, and mineralogical investigation of the chromitites and their host ultramafic rocks. These data are used to define the petrological processes in the mantle that created the protoliths of the Bir Tuluhah ophiolite. Our interpretation highlights the role of melt-rock reactions in the generation of high-Cr podiform chromitites.

2. Geological outline and field observations

The Bir Tuluhah area lies in the north-central part of Saudi Arabia, ~250 km south of Hail town (Fig. 1). It sits at the northern end of the elongated Al Hulayfa-Ad Dafina-Ruwah suture zone (HADRz), one of the longest proposed suture zones in Saudi Arabia. Although previous workers have correlated the HADRz with the Nabitah suture zone, suggesting that it was originally a 1200 km single structure now offset by left-lateral motion on the Ruwah Fault Zone (Quick, 1991), we prefer the newer view that these are different structures (Flowerdew et al., 2013). Hence the string of ophiolite complexes defining the HADRz marks only the boundary between the Afif and Hijaz terranes of the northern Arabian Shield (Fig. 1).

The study area has low relief, mostly flat-lying with small hills (< 50 m height). It lies between longitudes 25° 35\ and 25° 45\ E and latitudes 40° 45\ and 41° 00\ N. Map-scale units (Fig. 2) exposed in the area are all Neoproterozoic in age except for Wadi alluvial deposits. They include ophiolitic rocks, the Nagea volcaniclastics, the Shammar group, the Hulayfah group, amphibolite and the Shammar intrusive suite (granitoids, gabbro and diorite). The contacts between these units are invariably steeply dipping faults and the sequence is disrupted in many places. The area is furthermore dissected by two sets of faults, namely the older north-northeast

trending Al Hulayfah-Ad Dafina fault system and the younger northwest trending Najd fault system (Delfour, 1977; Johnson and Kattan, 2001). The faults obscure the original stratigraphic and structural relations of the different lithologic units in the mapped area.

The ophiolitic rocks of Bir Tuluhah are well exposed in the middle part of the mapped area (Fig. 2). They form an elongated belt in the N-S direction (~ 15 km long) as well as small scattered outcrops (< 2 km long). We define the dismembered ophiolite complex to include only the units mapped as serpentinized peridotite and layered gabbro, along with some small masses of plagiogranite. They occur as strongly folded allochthonous thrust sheets sheared along a subvertical brittle-ductile shear zone and tectonically interpalated between metasedimentary and metavolcanic units (Kattan, 1983; Quick and Bosch, 1990; Johnson and Kattan, 2001).

Structurally, the Bir Tuluhah ophiolite exhibits multiple phases of folding and shearing. Most of the serpentinite is foliated and mylonitized, with strong cataclastic textures. However, lenses of massive serpentinite with preserved primary textures are found within the highly foliated serpentinite. These lenses range from a less than a meter to hundreds of meters in length. Structural relations and shear sense indicators demonstrate that the serpentinite was obducted over the amphibolite and metamorphosed volcaniclastic units now exposed along their eastern side due to east-west compression east-directed over thrusting (Quick and Bosch, 1990). That is, we do not believe the structural relations are consistent with the grouping of the serpentinites, amphibolites, and metavolcanic units into a single island-arc package as interpreted by Delfour (1977). Along shear zones, the serpentinites are highly altered to quartz-carbonate (listvenite), talc-carbonate, secondary amphibole, and chlorite-bearing varieties.

The serpentinite is cut by dykes of different compositions including diabase, diorite, gabbro and plagiogranite. These dykes are disrupted and have suffered from various degrees of

recrystallization and alteration, suggesting that they were emplaced over a significant time span. Diabase, gabbro and anorthosite dykes are surrounded by well-developed black-wall reaction zones that formed during serpentinization of the peridotite wall rocks. Some of these dykes are highly deformed and completely recrystallized to rodingite, although some of them still preserve primary igneous mineralogy in the interiors. By contrast, the diorite dykes are undeformed and show little evidence of black-wall reaction or rodingitization, suggesting that they were emplaced after complete serpentinization of the peridotite.

Chromitite ores in the area may be massive or sheared and exhibit a range of shapes and sizes including pods, lenses, thin layers and schlieren (Al-Shanti and El-Mahdy, 1988, Habtoor et al., 2017). Massive chromitite lenses and pods are mainly restricted to the northernmost part of the band of serpentinites. Chromitite bodies form prominent outcrops as a result of their resistance to weathering. They may be isolated or in clusters. They are concordant to the foliation in the surrounding serpentinized peridotite and typically elongated parallel to the N-S trend of the serpentinite belt. Chromitite bodies vary in length from 0.5 m to more than 10 m. They mostly have relatively sharp contacts with the surrounding serpentinites but in some cases the boundaries of the chromitites are diffuse.

The layered gabbro occurs in a narrow band west of the main serpentinite band (Fig. 2). It is highly deformed and metamorphosed and layered on scales from centimeters to meters (Le Metour et al. 1983). Although the contact between layered gabbro and serpentinite is a fault, we map both these distinctively ophiolitic units as the Bir Tuluhah ophiolite.

To the east of both serpentinite masses, outcrops of amphibolite are confined to thrust planes. These rocks have strongly schistose textures and they lack any clear primary textures or relict mineralogy to identify their protoliths. While it is possible that the coarse-grained

amphibolite is the result of amphibolite facies metamorphism of ophiolitic gabbro, this would require complex structural relations to emplace metagabbro structurally below the serpentinite and these is no chemical, textural, or mineralogic evidence to support this idea.

The Nagea volcaniclastics include chert, fine-grained sandstone, interbedded felsic tuff and minor pillowed metabasalt. The association of pillowed metabasalt with felsic tuffs and sandstone suggest that this sequence is not related to the ophiolite, but instead represents a volcanic arc association. The metabasalt is fine-grained, light gray to gray-green, and its original structure and texture have been virtually obliterated by metamorphism.

The Hulayfah group covers the entire western part of the mapped area. It consists of volcano-sedimentary successions including mainly basalt and andesite and their pyroclastic equivalents (andesitic tuff and basaltic breccia) overlain by metasedimentary rocks. The metasediments include interbedded volcanogenic sandstone and shale with lenses of blue marble. The sandstone is poorly sorted and contains fragments of volcanic rocks partly derived from the underlying basalt. The marble lenses are common throughout the stratigraphical sequence of the Hulayfah group. Some marble masses contain serpentinite fragments, suggesting they may actually have formed by carbonate replacement of peridotite. Other marble bodies are bedded, indicating that they are sedimentary in origin.

The Shammar group, exposed in the northeastern corner of the study area, consists of basalt unconformably overlain by epiclastic rocks. The epiclastic rocks outcrops form a series of low hills featuring poorly sorted conglomerate overlying basalt. The clasts in the conglomerate include plutonic (diorite, granodiorite, syenogranite and alkali-feldspar granite) and volcanic (diabase and granophyre) rock fragments. The uppermost unit in the group consists of red-weathering rhyolitic rocks.

The Shammar intrusive suite includes granitoids, diorite and fresh gabbro. The granitoids mapped as undifferentiated rocks including mainly monzogranite and syenogranite with local alkali granite and granodiorite. The diorite is exposed as an undeformed pluton containing xenoliths of amphibolite and intruding the southern and central parts of the ophiolite. The diorite intrusion crosscuts the Al Hulayfah and Ad Dafina fault system and is in turn crosscut by a northwest-trending set of faults recognized as part of the Najd fault system (Delfour, 1977; Johnson and Kattan, 2001). A fresh gabbro pluton occurs in a narrow band to the west of the layered gabbro. This unit intrudes and postdates the ophiolitic metagabbro. It is fresh, undeformed, unmetamorphosed, and clearly not part of the ophiolite sequence.

There are a number of geochronological constraints that define approximate ages for the Neoproterozoic rocks of the Bir Tuluhah area. Pallister et al. (1987) report U-Pb model ages of 823±11 Ma and 847±14 Ma for zircons separated from plagiogranite dykes that cut the serpentinite south of Bir Tuluhah. These two ages provide a minimum age for the ophiolite and are taken to establish the lower age limit for the ultramafic protoliths of the serpentinite. The development of rodingite and blackwall reaction around the plagiogranite dykes indicates that significant serpentinization and deformation occurred after their intrusion. Also, Delfour (1977) interprets K-Ar isotopic data for the Hulayfah Group to indicate primary crystallization at 740 Ma with a partial resetting event at 577-563 Ma. The age of the Hulayfah Group is also weakly constrained by a U-Pb zircon age of 720±10 Ma obtained from tonalite that intrudes the formation west of the Hulayfah fault zone (Calvez et al., 1983). A low-quality U-Pb zircon age of 750-710 Ma from three discordant zircons from a quartz diorite pluton intruded into the Ad Dafina ophiolite to the south of the study area along the suture zone is interpreted as a minimum age for the formation of the amphibolite, metabasalt, and metatuff, and for the initiation of

Nabitah faulting. Also, it constrains the minimum age for ophiolite deformation and alteration (Quick, 1991). Delfour (1977) reports an age of 570 Ma for a small granophyre plug northwest of Bir Tuluhah. This age is interpreted to be a lower limit for the cessation of Al Hulayfa-Ad Dafina faulting since strands of the fault system are truncated by granitic rocks of similar composition throughout the area. Thus, field relations and available geochronological data indicate motion on the north-trending suture zone faults in the study area began after ~823 Ma but before ~710 Ma and ceased prior to ~570 Ma. Crosscutting relationships suggest that emplacement of mafic and intermediate intrusive rocks was synkinematic with motion on the suture fault system. Later offset by left-lateral strike-slip motion on the Najd faults postdates 570 Ma.

3. Petrography

3.1. Serpentinized peridotite

Although the Bir Tuluhah mantle section is highly serpentinized, the original protoliths can be recognized from preserved textures; they include harzburgite and dunite. Serpentinized harzburgite is dark green and its degree of alteration increases slightly near chromitite ore bodies. Textural observation indicates their original mode consisted essentially of olivine (60–80 vol. %) and orthopyroxene (20-40 vol. %). The pyroxenes and olivine are completely replaced by serpentine, magnetite, carbonates, brucite and minor talc. The serpentine is mainly antigorite with sparse veins of chrysotile (Fig. 3a). Orthopyroxene has been replaced by serpentine to form bastite, while olivines form mesh texture (Fig. 3b). Some bastite domains preserve the shape of plastically deformed orthopyroxene, indicating high temperature deformation of the protolith peridotite. Surviving relics of primary minerals are mostly Cr-spinel with rare olivine and pyroxene. The olivine relics (Fig. 3c) record notable strain features such as kink banding and

wavy extinction. Cr-spinel in harzburgite occurs as small subhedral to amoeboid grains or as chains of subhedral Cr-spinels.

Dunite forms lenses and envelopes around chromitite lenses. Dunite is brown-black to yellowish-brown in color and consists of aggregates of serpentine minerals with well-developed mesh texture derived from the original olivine. Sparse (<5 vol. %) areas of bastite texture formed after orthopyroxene are observed. Rare porphyroblastic and porphyroclastic textures are noted and fresh relics of olivines exhibit wavy extinction and kink bands. Cr-spinel occurs as randomly scattered anhedral to euhedral grains throughout the rock; however, they are locally sufficiently concentrated to form disseminated chromitite (Fig. 3d). In places the margins of chromite grains are replaced by magnetite but the cores preserve primary Cr-spinel compositions.

3.2. Chromitite

Chromitite occurrences in the study area are mostly small bodies and be either massive or sheared. The massive chromitites are usually fresh and composed mainly of subhedral to anhedral chromite grains with minor interstitial minerals (Fig. 3e). The sheared chromitite has the same composition as the massive type but the Cr-spinels are stretched and arranged in a preferred orientation to produce a schistose foliation (Fig. 3f). The amounts of Cr-spinel in both chromitites range from 92–98 vol. % with grain sizes ranging from 2 to 20 mm. The interstitial matrix of the chromitites mainly consists of serpentine minerals with accessory carbonates, chlorite and sulphides. Very small inclusions of silicate minerals including olivine are observed within the Cr-spinels and traces of intergranular or fracture-filling chlorite can be found. Cumulate, chain structures and banding textures, typical of magmatic crystallization (Pal and Mitra, 2004), are common. The massive chromitite pods are affected by variable amounts of deformation and

cracking; the cracks apparently acted as channels for migration of fluids that led to minor alteration of Cr-spinel to ferritchromite along the cracks. Nevertheless, the massive chromitites are less altered than the chromite grains in the host serpentinites.

4. Mineral chemistry

Surviving primary olivine and Cr-spinel from serpentinized peridotite and chromitite samples from Bir Tuluhah were analyzed using a five-spectrometer JEOL JXA-8200 electron microprobe at the Division of Geological and Planetary Sciences (GPS), California Institute of Technology. The analytical conditions were 15 kV accelerating voltage, 25 nA beam current, a focused beam diameter (1 μm) and 20 seconds on-peak counting times. Selected additional polished thin sections were analyzed using a JEOL JXA-8500F electron microprobe housed at Washington State University, with a similar protocol except for 20 nA beam current. Primary standards were all synthetic minerals, notably synthetic forsterite (Mg, Si), fayalite (Fe), Mn-olivine (Mn), anorthite (Ca, Al), Cr_2O_3 (Cr), NiO (Ni), and TiO_2 (Ti). Representative microprobe data of olivines and Cr-spinel are presented in Tables (1-4), while the whole data set of microprobe analyses is given in the supplementary Tables (1S-5S).

4.1. Serpentinized peridotite

Relics of primary olivine and Cr-spinel were analyzed from both serpentinized harzburgite and dunite. Representative microprobe analyses of olivine and corresponding calculated structural formulae are given in Table 1 and the full data set for olivine is given in Supplementary Tables 1S and 2S. The olivines analyses all yield low concentrations of TiO_2 (<0.01 wt. %), Cr_2O_3 (<0.03 wt. %), Al_2O_3 (<0.01wt. %) and CaO (< 0.04 wt. %). Olivine in

harzburgite has lower forsterite content, Fo_{90-91}, and NiO (0.37-0.46 wt. %) than in dunite (Fo_{92-93} and 0.44-0.52 wt. % NiO). Fo and NiO contents in olivine harzburgite plot on the mantle olivine array (Takahashi et al., 1987), whereas olivine from dunite has more NiO at a given Fo content than is expected for residual olivines from the mantle (Fig. 4a). Both harzburgite and dunite olivine NiO and Fo contents plot within the range of previously published analyses from ophiolites of the ANS.

Fresh relics of Cr-spinel were analyzed in both serpentinized harzburgite and dunite; thin secondary magnetite rims were not analyzed. Representative chemical compositions and structural formulae of primary Cr-spinels are given in Table 2, and the whole data set is given in Supplementary Tables 3S and 4S. The Cr# [molar Cr/(Cr+Al)] and Mg# [Molar Mg/(Mg+Fe^{2+})] of fresh Cr-spinel cores are higher in dunite (Cr# = 0.67-0.72 and Mg# = 0.59-0.73) than in harzburgite (Cr# = 0.58-0.65 and Mg# = 0.54-0.60). Cr-spinel from harzburgite plots in the region of Cr#-Mg# space commonly found in fore-arc peridotites (Fig. 4b), whereas Cr-spinel in dunite trends out of the fore-arc region towards the boninite field (Dick and Bullen, 1984; Bloomer et al., 1995; Ohara et al., 2002). In general, boninite is characteristic of intra-oceanic fore-arcs (e.g., Beccaluva et al., 2004; Dilek et al., 2008), supporting a fore-arc setting for the ultramafic rocks of Bir Umq. All the analyzed fresh Cr-spinel cores have low or negligible Fe^{3+}# = Fe^{3+}/(Fe^{3+}+Cr+Al) < 0.03, which is characteristic of primary mantle-derived spinels (Hattori and Guillot, 2007; Gahlan et al., 2015; Obeid et al., 2016; Bernstein et al., 2013; Azer, 2014). Note that in some cases the charge balance calculation to estimate Fe^{3+} from electron probe data by seeking a formula with four oxygens per three cations yields slightly negative apparent Fe^{3+}. This should be interpreted as Fe^{3+} within error of zero and possibly indicates small systematic errors in the probe analysis of spinel. In these cases all Fe in the structural formula occurs as Fe^{+2}

(Droop, 1987). The high Cr# (0.58-0.72) and low TiO_2 (≤ 0.13 wt. %) of the Cr-spinel are similar to spinel analyses from samples of depleted to highly depleted residual mantle that has experienced high degrees of partial melt extraction (e.g. Uysal et al., 2012) (Fig. 3a). Cr-spinel grains in the serpentinized harzburgite and dunite do show a well-developed chemical zoning, but this feature is not the target of the present work.

4.2. Chromitite

Fresh cores of Cr-spinel crystals and their mineral inclusions in the massive chromitite were analyzed. Chemical zoning is very limited in the chromitite spinel; local thin rims of ferritchromite along grain boundaries and cracks can be observed but these areas were not analyzed. Selected analyses are presented in Table 3 and the whole data set is given in Supplementary Table 5S. The Cr-spinel in the chromitite has very high Cr#, mostly from 0.71 to 0.81, and Mg# overlapping values from dunite, 0.59 to 0.72. The Cr-spinel analyses from chromitite extend into the regions of the Cr#-Mg# and Cr#-TiO_2 plots associated with boninite (Fig. 4b).

Six primary olivine inclusions within fresh Cr-spinel in chromitite were located and analyzed. Their compositions and structural formulae are given in Table 4. Although the inclusions are small, there is no evidence in their analyses for contamination by secondary fluorescence or beam overlap with host Cr-spinel. They are highly magnesian ($Fo_{94–95}$) and have elevated NiO (0.55–0.85 wt.%) alongside low CaO (<0.05 wt.%) and MnO (<0.1 wt.%). The Fo and NiO contents of these olivine inclusions in chromitite are distinctly higher than those of olivine in either harzburgitic or dunitic host rock (Tables 1 and 4).

5. Discussion

5.1. Tectonic setting

Ophiolitic rocks represent remnants of upper mantle and ancient oceanic crust, which are tectonically emplaced onto continental margins during closing of ocean basins. They were emplaced in a variety of tectonic settings, from the rift–drift and seafloor spreading stages to subduction initiation and terminal closure (Dilek and Furnes, 2014; Furnes et al., 2014).They show great variations in their internal structure, emplacement mechanisms, tectonic environments and geochemical characteristics (Dilek et al., 2008; Dilek and Furnes, 2014).

The Arabian Shield ophiolites represent an important source of evidence for reconstructing the geodynamic evolution of the ANS and the larger Pan-African belt. Published works have concluded that the ophiolites of Saudi Arabia formed in a variety of tectonic settings, ranging from mid-ocean ridge (MOR) to supra-subduction zone (SSZ) settings (e.g.Habtoor et al., 2017; Abuamarah, 2019 a,b; Gahlan et al., 2020), but most recent studies have preferred a SSZ setting for Arabian Shield ophiolites (e.g. Nassief et al., 1984; Pallister et al., 1988; Stern et al., 2004; Habtoor et al., 2017; Abuamarah, 2019 a,b; Gahlan et al., 2020). Furthermore, seafloor spreading in the vicinity of a subduction system can form ophiolite sequences in both fore-arc and back-arc environments (Pearce, 2003; Azer and Stern, 2007); the distinctions between ophiolites formed in these particular settings have been increasingly recognized recently. The mantle sections of MOR ophiolites typically include both harzburgite and lherzolite with subordinate dunite, whereas SSZ ophiolites are dominated by harzburgite (80%–90%), typically with minor dunite, lherzolite, or pyroxenite (Pearce et al., 1984). Hence, the first-order petrographic and mineralogical observations of the Bir Tuluhah ultramafic rocks, which are

exclusively harzburgite and dunite with no lherzolite protoliths, already imply a likely SSZ affinity.

At a more detailed level, the mineral chemistry of primary Cr-spinel, olivine, and pyroxene provide important information about factors controlling peridotite evolution, such as extent of melting and melt-rock reaction, composition of extracted or transiting melts, the presence of water, the oxidation state of the system, and more (Takahashi et al., 1987; Rollinson 2008; Ohara et al., 2002; Arif and Jan, 2006; Uysal et al., 2012). In the present case, as pointed out above, accessory fresh Cr-spinels in the serpentinized harzburgites at Bir Tuluhah plot in the field of depleted fore-arc peridotites (Figs. 4b and 5a), lending additional support to the SSZ affinity of the suite (e.g. Dick and Bullen, 1984; Bonatti and Michael, 1989; Azer and Stern, 2007). Furthermore, on the Al_2O_3 vs. Fe^{2+}/Fe^3 diagram (Kamenetsky et al., 2001), the fresh Cr-spinels in the serpentinized peridotites plot again in the SSZ peridotite field (Fig. 5b). The compositions of fresh olivine relics in the serpentinized peridotites are magnesium and nickel-rich and resemble olivine from mantle residues that underwent extensive partial melt extraction, most commonly seen in fore-arc settings (e.g. Pearce et al., 2000; Coish and Gardner, 2004).

5.2. Chromitite petrogenesis

The origin of chromitite ores has attracted a great deal of attention and remains a matter of debate. Chromitites occur as podiform or stratiform masses within residual and cumulate mantle peridotites, respectively. Podiform chromitites occur as discontinuous pod-shaped bodies, either concordant or discordant with surrounding ophiolitic dunites and harzburgites (Miura et al., 2012; Khedr and Arai, 2017). The genesis of podiform chromitites in various tectonic settings has been a subject of considerable controversy for many years (e.g. Roberts, 1988; Matveev and

Ballhaus, 2002; Habtoor et al., 2017; Khedr and Arai, 2017). The most accepted mechanism for the formation of podiform chromitite is melt-peridotite interaction and subsequent mixing (e.g. González-Jiménez et al., 2011, 2014; Arai and Miura, 2016; Khedr and Arai, 2017; Azer et al., 2019). Through this mechanism, the formation of chromitite pods begins with interaction between ascending melt and overlying refractory mantle harzburgite through which the melt percolates in large conduits. Subsequent mixing of this secondary melt with a new influx of primitive melt results in a hybrid melt oversaturated with spinel component and subsequent precipitation of chromite (e.g., Roberts, 1988; Arai and Abe, 1995). In massive chromitites, subsolidus equilibration of chromite with surrounding silicates generally occurs to a very limited extent, if at all (Suita and Streider, 1996). Hence, they preserve pristine late magmatic compositions and evidence bearing on the primary melts from which they precipitated. Therefore, chromitite mineral chemistry may be key to understanding the tectonic setting in which the chromitites and their host mantle peridotites formed and to tracing the processes that form mantle lithosphere (Dick and Bullen, 1984; Kamenetsky et al., 2001; Arai et al., 2006; Rollinson, 2008; Pagé and Barnes, 2009).

Because the composition of melt in equilibrium with peridotite minerals shifts with pressure, migration of melt leads to disequilibrium between the ascending melt and the minerals along the conduit. Most commonly, the expansion of the olivine phase volume with decreasing pressure causes pyroxenes in harzburgite to dissolve and olivine to precipitate in response to reaction with migrating melts, leading eventually to replacive dunite (e.g. Kelemen, 1990; Azer et al., 2019). The association of massive chromitite with such dunite shows that both rock types form at successive stages of evolution of shared melt migration conduits (c.f. Zhou et al., 1996; Melcher et al., 1997), often in the depleted mantle sections of SSZ ophiolites (Ballhaus, 1998;

Melcher et al., 1999; Uysal et al., 2016). In general, as the reaction of ascending mantle melts with wall-rock peridotites precipitates olivine and forms a dunite envelope, the melt becomes increasing enriched in Si and Cr. This melt can react with new batches of primitive magma to form boninitic melts oversaturated with Cr that then precipitate chromitite pods.

The high water contents of the melts that migrate through SSZ mantle may be a key factor in chromitite formation (Edwards et al., 2000; Matveev and Ballhaus, 2002; Mondal et al., 2006). Experimental results on water-bearing basalts suggest that ophiolitic chromitites form only when primitive melts are saturated in olivine + chromite and also rich in water (Matveev and Ballhaus, 2002).

Discussions of the origin and geotectonic setting of chromitite ore bodies in general have been echoed by specific debate about the podiform chromitites of the ANS (e.g. Habtoor et al., 2017; Khedr and Arai, 2017). Podiform chromitites from the Arabian Shield are commonly enveloped by dunite within the generally harzburgite-dominated depleted mantle section (e.g. Habtoor et al., 2017), consistent with the wall-rock interaction mechanism for their formation (Zhou et al., 2005; González-Jiménez et al., 2011, 2014). At Bir Tuluhah as well, we observe podiform massive chromitites with dunite envelopes surrounded by gradational contacts to harzburgite.

The suggested model for formation of the Bir Tuluhah chromitite pods begins with formation of a depleted mantle section dominated by harzburgite. The high Cr# of even the least affected spinels in the host harzburgites indicate that the degree of melt extraction experienced at this stage was large (e.g. Rollinson, 2008; González-Jiménez et al., 2011). Subsequently, ascending hydrous melts coming from below formed channelized conduits as their reactions with the harzburgite dissolved orthopyroxene, concentrated olivine, and increased the melt flux and

permeability. The end products of this reaction were conduits of dunite occupied by re-equilibrated silica and chromium-rich melt. Once orthopyroxene was exhausted from the conduit, it could no longer buffer the melts to high silica activity and subsequent influxes of primitive melt would remain Mg-rich. Mixing of primitive melt with the reaction-product melt resulted in a hybrid melt of boninitic affinity (rich in both Si and Mg) and oversaturated with the components of Cr-spinel, which was then precipitated. The extremely Mg-rich olivine inclusions in the chromitites may testify to the high melt fractions and elevated Mg-contents that governed this stage of the process, however their small size and contact with comparatively large volumes of Cr-spinel would have allowed ample opportunity for subsolidus re-equilibration to shift their composition without much affecting the chromite, so the olivine compositions should be interpreted only with some caution.

In the Bir Tuluhah case, the composition of Cr-spinel in dunite lies in between that in the podiform chromitites and in the host harzburgites. Cr# and Mg# in spinel both increase from the harzburgite through the dunite to the chromitite. This is consistent with the model of increased intensity of melt-rock reaction in the chromitite (e.g. Zhou et al., 1996). Furthermore, the affinity of the spinel chemistry in the chromitites with the fields of spinel from boninites in Cr#, Mg#, and TiO_2 content indicates a role for hydrous melt infiltration and a fore-arc supra-subduction zone setting for the Bir Tuluhah ophiolite (Figs. 4b, 5a, b). It has been argued before that boninite is the dominant parental magma for podiform chromitite deposits in ophiolites (Barnes and Roeder, 2001). The notably lower Fe^{2+}/Fe^{3+} values in spinels from the chromitite pods compared with their host peridotites may also indicate that the infiltrating melt that formed the chromitites was substantially more oxidizing than the mantle it infiltrated (Kamenetsky et al., 2001; Deschamps et al., 2013).

5.3. A quantitative thermodynamic model

The origin of podiform chromitite by mixing of reacted, silica-rich melt and unreacted, Mg-rich hydrous melt has been suggested by previous authors on the basis of experimental evidence (Matveev and Ballhaus 2002), use of simplified phase diagrams (Irvine, 1977; Aria and Miura, 2016), and abundant field evidence (Roberts, 1988; Arai and Abe, 1995). Here, for the first time, we apply an internally-consistent thermodynamic model of the multicomponent phase relations to examine this hypothesis. We use the latest version of the MELTS model (Ghiorso and Sack, 1995) and perform calculations with the alphaMELTS interface (Smith and Asimow, 2005), which includes a method for accounting for the effects of trace H_2O in the mantle during decompression melting (Asimow et al., 2004). Previous work has shown how to use MELTS to construct useful forward models of both (a) the polybaric near-fractional melting process that forms complementary depleted harzburgite and primary aggregate basalt (Asimow et al., 2001; Asimow and Longhi, 2004) and (b) the equilibrium porous flow process that forms dunite conduits and their reacted melts (Asimow and Stolper, 1999). Therefore, in order to begin from a well-defined starting point for this model, we generate plausible end-member liquids for the mixing model using these two well-established calculations.

Following Asimow et al. (2001, 2004), we modeled the formation of a primary near-fractional aggregate melt, formed by mixing all the melts produced from the solidus down to 1 GPa pressure, often thought to be the last pressure at which typical primitive mid-ocean ridge basalt last equilibrated with residual orthopyroxene (Kelemen et al., 1995). The initial mantle source is the "High-Na" depleted mid-ocean ridge source model of Workman and Hart (2005), assumed to have 150 ppm H_2O present at depth as trace hydrogen in the major mantle minerals.

The temperature is adjusted so that this material encounters its "damp" solidus at 3.3 GPa. Near-fractional decompression melting of this source from this solidus that continued down to 0.1 GPa would yield, from 100 g of source, ~19 g of basaltic melt and a harzburgite residue containing 59 g of olivine, 20 g of orthopyroxene, and 2 g of spinel. Indeed, the calculation was continued down to 0.1 GPa in order to generate a depleted harzburgite residue composition for use in the next step. The composition of the integrated melt at 1 GPa is shown in Table 5; it is a primitive low-SiO_2 tholeiitic basalt liquid, with 46.6 wt.% SiO_2, 13.4 wt.% MgO, 0.045 wt.% Cr_2O_3, and 0.09 wt.% H_2O. This will be one end-member of the mixing model.

Next, following Asimow and Stolper (1999), we modeled the formation of a dunite conduit and its reacted liquid by equilibrating the above liquid with the 0.1 GPa harzburgite residue, at 0.1 GPa and the same temperature that resulted from the isentropic decompression melting proceeding to that point (1309.8 °C), gradually adding more and more melt to the residue until orthopyroxene was exhausted. This reaction progressively increased the $SiO2$, Cr_2O_3, and H_2O contents of the liquid, while keeping MgO nearly constant. The resulting liquid is a boninite, with 55.4 wt.% SiO_2, 13.7 wt.% MgO, 0.37 wt.% Cr_2O_3, and 1.42 wt.% H_2O. This will be the other end-member of the mixing model.

Both of the end-member liquids described above have olivine as their liquidus mineral at 0.1 GPa, closely followed by Cr-spinel. We explored a range of mixing ratios between them and determined the crystallization sequence of each mixture. Figure 6 plots the temperature of appearance of Cr-spinel and of olivine, as well as contours of mass fraction of Cr-spinel crystallized, against the SiO_2 contents of the mixtures. The model is a success, in that a "dome" of stability of Cr-spinel on the liquidus emerges above the olivine liquidus in the range between ~51 and 55 wt.% SiO_2, i.e. between ~5% and ~50% addition of the unreacted liquid to the reacted

liquid. If the temperature of the unreacted liquid is high enough that the mixture forms above the liquidus, indeed these liquids would crystallize monomineralic Cr-spinel for an interval of up to 3 °C before again becoming saturated with olivine. However, the process is not especially efficient. At some level, it could never be very efficient in terms of mass of spinel crystallized per mass of liquids mixed, since the boninitic liquid only contained 0.37 wt.% Cr_2O_3 to begin with. But the efficiency is much lower than that; a maximum of 0.012 g of Cr-spinel can form from 100 g of liquid, for the optimal mixture with 53 wt.% SiO_2 in the liquid. In other words, to form 1 g of pure Cr-spinel by this mechanism requires processing 8.3 kg of melt.

6. Summary

- The Neoproterozoic Bir Tuluhah ophiolite is a dismembered fragment of oceanic lithosphere obducted onto the Arabian continental margin following the closure of the Mozambique Ocean. Only an upper mantle section and a thin unit of layered gabbro are preserved.
- The mantle section of the Bir Tuluhah ophiolite comprises harzburgite and minor dunite tectonized by high-temperature deformation, based on preserved textures in the serpentinites. Associated with the dunites there are lenticular pods of chromitite of various sizes.
- Rare fresh relics of olivine and Cr-spinel were studied in serpentinized harzburgite and dunite. The abundant fresh Cr-spinel and rare fresh olivine inclusions in spinel were studied in the chromitites.
- Olivine in harzburgite and dunite have Fo and NiO contents consistent with those of residual mantle olivines that underwent high degrees of partial melt extraction. Olivine inclusions in chromitite lenses have even higher Fo and NiO contents, suggesting either continued melt infiltration and generation leading to chromitite genesis or subsolidus re-equilibration.

- Cr-spinel with the lowest Cr# is found in harzburgite and marks those samples least affected by melt-rock reaction. Spinel Cr# and Mg# continuously and systematically increase through the dunite samples and into the chromitites, indicating progressive melt-rock reaction processes leading to these lithologies.
- The harzburgite represents the residue of a first stage of melt extraction, while dunite represents melt-rock reaction with infiltrating melt and chromitite marks late mixing events between the melts residual to dunite formation and freshly infiltrated melt.
- A quantitative thermodynamic model confirms that mixing of two olivine-saturated liquids, one residual to dunite formation and one extracted from a harzburgite residue at higher pressure, while produce a chromite-saturated liquid, but the models suggests a low efficiency, precipitating 1 g of chromite from 8.3 kg of melt.
- The mineral chemistry in all the rock types is consistent with formation in a fore-arc supra-subduction zone and shows that they represent solid residues of processes that may have led to the eruption of characteristic fore-arc boninite lavas.

ACKNOWLEDGEMENTS

The authors would like to extend their appreciation and gratitude to the King Saud University for funding and supporting this work through Researchers Supporting Project number (RSP-2019/151), King Saud University, Riyadh, Saudi Arabia. PDA is supported by the US NSF award EAR-1826310. In addition, the authors highly appreciate thoughtful reviews by Prof. Hilmy E. Moussa and an anonymous reviewer. The authors are also indebted to the editor (Prof. Michael Roden) for his efforts and numerous helpful comments.

Declaration of Interest: None

References

Abuamarah, B.A., 2019a. Geochemistry and fore-arc evolution of upper mantle peridotites in the Cryogenian Bir Umq ophiolite, Arabian Shield, Saudi Arabia. International Geology Review (DOI: 10.1080/00206814.2019.1652942).

Abuamarah, B.A.,2019b. Petrogenetic evolution of Cryogenian Halaban ophiolite, Saudi Arabia: A fragment of fore-arc oceanic lithosphere mantle. Lithos (https://doi.org/10.1016/j.lithos.2019.105303.

Ahmed, Z., Hariri, M.M., 2008. Neoproterozoic ophiolites as developed in Saudi Arabia and their oceanic and pericontinental domains. Arabian Journal for Science and Engineering 33, 17-54.

Ali, K.A., Azer, M.K., Gahlan, H.A., Wilde, S.A., Samuel, M.D., Stern, R.J., 2010. Age of formation and emplacement of Neoproterozoic ophiolites and related rocks along the Allaqi Suture, south Eastern Desert, Egypt. Gondwana Research 18, 583-595.

Al-Shanti, A.M., El-Mahdy, O.R., 1988. Geological Studies and Assessment of Chromite Occurrences in Saudi Arabia: KACST Project No. AT-6-094.

Arai, S., Miura, M., 2016. Formation and modification of chromitites in the mantle. Lithos 264, 277–295.

Arai, S., Abe, N., 1995. Reaction of orthopyroxene in peridotite xenoliths with alkali basalt melt and its implication for genesis of alpine-type chromitite. American Mineralogist 80, 1041–1047.

Arai, S., Shimizu, Y., Ismail, S.A., Ahmed, A.H., 2006. Low-T formation of high-Cr spinel with apparently primary chemical characteristics within podiform chromitite from Rayat, northeastern Iraq. Mineralogical Magazine 70, 499–508.

Arif, M., Jan, M.Q., 2006. Petrotectonic significance of the chemistry of chromite in the ultramafic-mafic complexes of Pakistan. Journal of Asian Earth Sciences 27, 628-646.

Asimow, P.D., Longhi J., 2004. The significance of multiple saturation points in the context of polybaric near-fractional melting. Journal of Petrology 45(12), 2349-2367.

Asimow, P.D., Stolper, E.M.,1999. Steady-state mantle-melt interactions in one dimension: I. Equilibrium transport and melt focusing. Journal of Petrology 40(3), 475-494.

Asimow, P.D., Dixon, J.E., Langmuir, C.H., 2004. A hydrous melting and fractionation model for mid-ocean ridge basalts: Application to the Mid Atlantic Ridge near the Azores. Geochemistry, Geophysics, Geosystems 5(1), Q01E16.

Asimow, P.D., Hirschmann M.M., Stolper, E.M., 2001. Calculation of peridotite partial melting from thermodynamic models of minerals and melts. IV. Adiabatic decompression and the composition and mean properties of mid-ocean ridge basalts. Journal of Petrology 42(5), 963-998.

Azer, M.K., 2014. Petrological studies of Neoproterozoic serpentinized ultramafics of the Nubian Shield: Spinel compositions as evidence of the tectonic evolution of the Egyptian ophiolites. Acta Geologica Polinica 64, 113–127.

Azer, M.K. and Stern, R.J., 2007. Neoproterozoic (835-720 Ma) serpentinites in the Eastern Desert, Egypt: Fragments of fore-arc mantle. The Journal of Geology 115, 457–472.

Azer, M.K., Gahlan, H.A., Asimow, P.D., Al-Kahtany, K.M., 2017. The Late Neoproterozoic Dahanib mafic-ultramafic intrusion, South Eastern Desert, Egypt: is it an Alaskan-type or a layered intrusion? American Journal of Science 317, 901-940.

Azer, M.K., Gahlan, H.A., Asimow, P.D., Mubarak, H.S., Al-Kahtany, K.M., 2019. Multiple stages of carbonation and element redistribution during formation of ultramafic-hosted

magnesite in Neoproterozoic ophiolites of the Arabian-Nubian Shield, Egypt. The Journal of Geology 127(1), 81-107.

Ballhaus, C., 1998. Origin of podiform chromite deposits by magma mingling. Earth and Planetary Science Letters 156(3-4),185-193.

Barnes, S.J. and Röeder, P.L., 2001. The range of spinel compositions in terrestrial mafic and ultramafic rocks. Journal of petrology 42, 2279–2302.

Beccaluva, L., Coltori, M., Giunta, G., Siena, F., 2004. Tethyan vs. Cordilleran ophiolites: a reappraisal of distinctive tectono-magmatic features of supra-subduction complexes in relation to subduction mode. Tectonophysics 393, 163-174.

Bernstein, S., Szilas, K., Kelemen, P.B., 2013. Highly depleted cratonic mantle in West Greenland extending into diamond stability field in the Proterozoic. Lithos 168–169, 160–172.

Bloomer, S.H., Taylor, B., MacLeod, C.J., Stern, R.J., Fryer, P., Hawkins, J.W., Johnson, L., 1995. Early arc volcanism and ophiolite problem: A perspective from drilling in the Western Pacific. In: Taylor, B., Natland, J. (Eds.), Active Margins and Marginal Basins of the Western Pacific. Geophysical Monograph, Vol. 88. American Geophysical Union, Washington, DC, pp. 1-30.

Bonatti, E., Michael, P.J., 1989. Mantle peridotites from continental rifts to oceanic basins to subduction zones. Earth and Planetary Science Letters 91, 297-311.

Boskabadi, A., Pitcairn, I.K., Broman, C., Boyce, A., Teagle, D.A.H., Cooper, M.J., Azer, M.K., Mohamed, F.H., Stern, R.J., Majka, J., 2017. Carbonate alteration of ophiolitic rocks in the Arabian–Nubian Shield of Egypt: sources and compositions of the carbonating fluid

and implications for the formation of Au deposits. International Geology Review 59(4), 391–419.

Caby, R., 1982. Petrological and structural observations from the Nuqrah area and some remarks concerning the crustal history of the northern Najd Province, Saudi Arabia: Pan-African crustal evolution in Arabia and northeast Africa (Al-Shanti, A. M., ed.). Precambrian Research 16, A11-A12.

Calvez, J.Y., Alsac, C., Delfour, J., Kemp, J., Pellaton, C., 1983. Geological evolution of western, central and eastern parts of the northern Precambrian Shield, Kingdom of Saudi Arabia: Saudi Arabian Deputy Ministry for Mineral Resources Open-File Report BRGM-OF-03-17, scale 1:100,000.

Coish, R.A., Gardner, P.,2004. Suprasubduction-zone peridotite in the northern USA Appalachians: evidence from mineral composition. Mineralogical Magazine 68, 699–708.

Delfour, J., 1977. Geology of the Nuqrah quadrangle, sheet 25E, Kingdom of Saudi Arabia: Saudi Arabian Directorate General of Mineral Resources Geologic Map GM-28, scale 1:250,000, 32 p.

Deschamps, F., Godard, M., Guillot, S., Hattori, K., 2013. Geochemistry of subduction zone serpentinites: a review. Lithos 178, 96–127.

Dick, H.J., Bullen, T., 1984. Chromian spinel as a petrogenetic indicator in abyssal and alpine-type peridotites and spatially associated lavas. Contributions to Mineralogy and Petrology 86(1), 54-76.

Dilek, Y., Ahmed, Z., 2003. Proterozoic ophiolites of the Arabian Shield and their significance in Precambrian tectonics, in Dilek Y. and Robinson P.T. (eds) Ophiolites in Earth History. Geological Society of London Special Publication 218, 685-700.

Dilek, Y., Furnes, H., Shallo, M., 2008. Geochemistry of the Jurassic Mirdita Ophiolite (Albania) and the MORB to SSZ evolution of a marginal basin oceanic crust. Lithos 100(1–4), 174-209.

Dilek, Y., Furnes, H., 2014. Ophiolites and Their Origins. Elements 10 (2), 93-100.

Droop, G.T.R., 1987. A general equation for estimating Fe^{3+} concentrations in ferromagnesian silicates and oxides from microprobe analyses, using stoichiometric criteria. Mineralogical Magazine 51(361), 431-435.

Edwards, S.J., Pearce, J.A., Freeman, J., 2000. New insights concerning the influence of water during the formation of podiform chromite. In: Dilek Y., Moores E. M., Elthon D., Nicolas A. (Eds.), Ophiolites and oceanic crust: New insights from field studies and the Ocean Drilling Program. Geological Society of America. Special Paper 349, 139-147.

Flowerdew, M.J., Whitehouse, M.J., Stoeser, D.B., 2013. The Nabitah fault zone, Saudi Arabia: A Pan-African suture separating juvenile oceanic arcs. Precambrian Research 239, 95-105.

Furnes, H., de Wit, M., Dilek, Y., 2014. Four billion years of ophiolites reveal secular trends in oceanic crust formation. Geoscience Frontiers 5, 571–603.

Gahlan, H.A., Azer, M.K., Khalil, A.E.S., 2015. The Neoproterozoic Abu Dahr ophiolite, South Eastern Desert, Egypt: Petrological characteristics and tectonomagmatic evolution. Mineralogy and Petrology 109, 611-630.

Gahlan, H.A., Azer, M.K., Asimow, P.D., Mubarak, H.S., Al-Kahtany, K.M., 2020. Petrological characteristics of the Neoproterozoic Ess ophiolite mantle section, Arabian Shield, Saudi Arabia: a mineral chemistry perspective. International Journal of Earth Sciences 109, 239-251.

Ghiorso, M.S., Sack, R.O., 1995. Chemical mass transfer in magmatic processes IV. A revised and internally consistent thermodynamic model for the interpolation and extrapolation of liquid-solid equilibria in magmatic systems at elevated temperatures and pressures. Contributions to Mineralogy and Petrology 119, 197-212.

González-Jiménez, J.-M., Griffin, W.L., Proenza, J.A., Gervilla, F., O'Reilly, S.Y., Akbulut, M., Pearson, N.J., Arai, S., 2014. Chromitites in ophiolites: how, where, when, why? Part II. A review and new ideas on the crystallization of chromitites. Lithos 189, 140–158.

González-Jiménez, J.M., Proenza, J.A., Gervilla, F., Melgarejo, J.C., Blanco-Moreno, J.A., Ruiz-Sánchez, R., Griffin, W.L., 2011. High-Cr and high-Al chromitites from the Sagua de Tánamo district, Mayarí-Cristal ophiolitic massif (eastern Cuba): Constraints on their origin from mineralogy and geochemistry of chromian spinel and platinum-group elements. Lithos 125(1-2), 101-121.

Habtoor, A., Ahmed, A.H., Harbi, H., 2016. Petrogenesis of the Alaskan-type mafic–ultramafic complex in the Makkah quadrangle, western Arabian Shield, Saudi Arabia. Lithos 263, 33-51.

Habtoor, A.M., Ahmed, A.H., Akizawa, N., Harbi, H., Arai, S., 2017. Chemical homogeneity of high-Cr chromitites as indicator for widespread invasion of boninitic melt in mantle peridotite of Bir Tuluha ophiolite, Northern Arabian Shield, Saudi Arabia. Ore Geology Reviews 90, 243–259.

Harbi, H.M., 2008. Geology and lihostratigraphy of ultramafic–mafic rocks and associated mineralization, Wadi Khamal area, Western Saudi Arabia. King Abdulaziz University Journal of Earth Sciences 19, 119–157.

Hargrove, U.S., Stern, R.J., Griffin, W.R., Johnson, P.R., Abdelsalam, M.G., 2006b. From island arc to craton: timescales of crustal formation along the Neoproterozoic Bi'r Umq Suture zone, Kingdom of Saudi Arabia. Saudi Geological Survey Technical Report SGS-TR-2006-6. 69 pp.

Hargrove, U.S., Stern, R.J., Kimura, J.I., Manton, W.I., Johnson, P.R., 2006a. How juvenile is the Arabian–Nubian Shield? Evidence from Nd isotopes and pre-Neoproterozoic inherited zircon in the Bi'r Umq suture zone, Saudi Arabia. Earth and Planetary Science Letters 252, 308–326.

Hattori, K.H., Guillot, S., 2007. Geochemical character of serpentinites associated with high- to ultrahigh-pressure metamorphic rocks in the Alps, Cuba, and the Himalayas: recycling of elements in subduction zones. Geochemistry, Geophysics, Geosystems 8, Q09010.

Irvine, T.N., 1977. Origin of chromitite layers in the Muskox intrusion and other stratiform intrusions: a new interpretation. Geology 5, 273–277.

Jan, M.Q., Windley, B.F., 1990. Chromian spinel–silicate chemistry in ultramafic rocks of the Jijal complex, northwest Pakistan. Journal of Petrology 31, 667–715.

Johnson, P.R., Kattan, F., 2001. Oblique sinistral transpression in the Arabian shield: the timing and kinematics of a Neoproterozoic suture zone. Precambrian Research 107(1-2), 117-38.

Johnson, P.R., Kattan, F.H., Al-Saleh, A.M., 2004. Neoproterozoic ophiolites in the Arabian Shield: Field relations and structure. Developments in Precambrian Geology 13, 129-162.

Kamenetsky, V.S., Crawford, A.J., Meffre, S., 2001. Factors controlling chemistry of magmatic spinel: an empirical study of associated olivine, Cr-spinel and melt inclusions from primitive rocks. Journal of Petrology 42(4), 655-671.

Kattan, F.H., 1983. Petrology and Geochemistry of the Tuluhah Belt, North East Arabian Shield (M.S. thesis). King Abdulaziz University, Jiddah.

Kelemen, P.B., 1990. Reaction between ultramafic rock and fractionating basaltic magma I. Phase relations, the origin of calc-alkaline magma series and the formation of discordant dunite. Journal of Petrology 31, 51–98.

Kelemen, P.B., Shimizu, N., Salters, V.J.M., 1995. Extraction of mid-ocean ridge basalt from the mantle by focused flow of melt in dunite channels. Nature 375, 747-753.

Khedr, M.Z., Arai, S., 2017. Peridotite-chromitite complexes in the Eastern Desert of Egypt: Insight into Neoproterozoic sub-arc mantle processes. Gondwana Research 52, 59-79.

Kröner, A., Linnebacher, P., Stern, R.J., Reischmann, T., Manton, W.I., Hussein, I.M., 1991. Evolution of Pan-African island arc assemblages in the southern Red Sea Hills, Sudan and in southwestern Arabia as exemplified by geochemistry and geochronology. Precambrian Research 53, 99–118.

Kusky, T.M., Abdelsalam, M., Tucker, R., Stern, R., 2003. Evolution of East African and related orogens, and the assembly of Gondwana. Precambrian Research 123, 81–344.

Le Metour, J., Johan, V., Tegyey, M., 1983. Geology of the ultramafic-mafic complexes in the Bi'r Tuluhah and Jabal Malhijah areas. Saudi Arabian Deputy Ministry for Mineral Resources Open-File Report BRGM-OF-03-40, 47 pp.

Matveev, S., Ballhaus, C., 2002. Role of water in the origin of podiform chromitite deposits. Earth and Planetary Science Letters 203(1), 235-243.

Melcher, F., Grum, W., Simon, G., Thalhammer, T.V., Stumpfl, E.F., 1997. Petrogenesis of the ophiolitic giant chromite deposits of Kempirsai, Kazakhstan: a study of solid and fluid inclusions in chromite. Journal of Petrology 38(10),1419-1458.

Melcher, F., Grum, W., Thalhammer, T.V., Thalhammer, O.A., 1999. The giant chromite deposits at Kempirsai, Urals: constraints from trace element (PGE, REE) and isotope data. Mineralium Deposita 34(3), 250-272.

Miura, M., Arai, S., Ahmed, A.H., Mizukami, T., Okuno, M., Yamamoto, S., 2012. Podiform chromitite classification revisited: a comparison of discordant and concordant chromitite pods from Wadi Hilti, northern Oman ophiolite. Journal of Asian Earth Sciences 59, 52–61.

Mondal, S.K., Ripley, E.M., Li, C., Frei, R., 2006. The genesis of Archaean chromitites from the Nuasahi and Sukinda massifs in the Sighbum Craton, India. Precambrian Research 148, 45–66.

Moore, T.A., Al-Rehaili, M.H., 1989. Geologic map of the Makkah quadrangle, Sheet 21D. Kingdom of Saudi Arabia. Saudi Arabian Directorate General for Minerals Resources. Jeddah. Map GM-107C, scale 1:250,000.

Nassief, M.O., Macdonald, R., Gass, I.G., 1984. The Jabal Thurwah upper Proterozoic ophiolite complex, western Saudi Arabia. Journal of Geological Society of London 141, 537–546.

Nehlig, P., Genna, A., Asfirane, F., 2002. A review of the Pan-African evolution of the Arabian Shield. GeoArabia 7, 103–124.

Obeid, M.A., Khalil, A.E.S., Azer, M.K., 2016. Mineralogy, geochemistry and geotectonic significance of the Neoproterozoic ophiolite of Wadi Arais area, south Eastern Desert, Egypt. Internal Geological Review 58, 687-702.

Ohara, Y., Stern, R.J., Ishii, T., Yurimoto, H., Yamazaki, T., 2002. Peridotites from the Mariana Trough: first look at the mantle beneath an active back-arc basin. Contribution to Mineralogy and Petrology 143, 1-18.

Page, P., Barnes, S.J., 2009. Using trace elements in chromites to constrain the origin of podiform chromitites in the Thetford Mines Ophiolite, Québec, Canada. Economic Geology 104, 997-1018.

Pal, T., Mitra, S., 2004. P–T–fO_2 controls on a partly inverse chromite bearing ultramafic intrusive: an evaluation from the Sukinda Massif, India. Journal of Asian Earth Sciences 22, 483–493

Pallister, J.S., Stacey, J.S., Fischer, L.B., Premo, W.R., 1987. Precambrian ophiolites of Arabia: U-Pb geochronology, Pb isotopic characteristics, and implications for continental accretion. Saudi Arabian Deputy Ministry for Mineral Resources Open-File Report USGS-OF-07-10. USGS Open-File Report 88-606.

Pallister, J.S., Stacey, J.S., Fischer, L.B., Premo, W.R., 1988. Precambrian ophiolites of Arabia: Geologic settings, U-BP geochronology, BP-isotope characteristics, and implications for continental accretion. Precambrian Research 38, 1-54.

Pearce, J.A., 2003. Subduction Zone Ophiolites. In Y. Dilek, S. Newcomb (eds) Ophiolite Concept and the Evolution of Geological Thought, GSA Special Paper 373, 269-294.

Pearce, J.A., Barker, P.F., Edwards, S.J., Parkinson, I.J., Leat, P.T., 2000. Geochemistry and tectonic significance of peridotites from the South Sandwich arc-basin system, South Atlantic. Contribution to Mineralogy and Petrology 139, 36–53.

Pearce, J.A., Lippard, S.J., Roberts, S., 1984. Characteristics and tectonic significance of supra-subduction zone ophiolites. In: Kokelaar, P. B. and Howells, M. F. (eds) Marginal basin geology. Geological Society of London, Special Publication 16, 77–94.

Quick, J.E., Bosch, P.S., 1990. Tectonic history of the northern Nabitah fault zone, Arabian Shield, Kingdom of Saudi Arabia. US Geological Survey (No. 90-316).

Quick, J.E., 1991. Late Proterozoic transpression on the Nabitah fault system—implications for the assembly of the Arabian Shield. Precambrian Research 53(1-2), 119-47.

Roberts, S., 1988. Ophiolitic chromitite formation: A marginal basin phenomenon? Economic Geology 83, 1034–1036.

Rollinson, H., 2008. The geochemistry of mantle chromitites from the northern part of the Oman ophiolite: inferred parental melt compositions. Contribution to Mineralogy and Petrology 156, 273–288.

Smith, P.M., Asimow, P.D., 2005. Adiabat_1ph: A new public front-end to the MELTS, pMELTS, and pHMELTS models. Geochemistry Geophysics Geosystems 6, Q02004.

Stern, R.J., Johnson, P.R., Kröner, A., Yibas, B., 2004. Neoproterozoic ophiolites of the Arabian-Nubian Shield. In: Kusky, T.M. (Ed.), Precambrian Ophiolites and Related Rocks. Developments in Precambrian Geology 13, 95–128. Amsterdam: Elsevier.

Suita, M., Strieder, A., 1996. Cr-spinels from Brazilian mafic-ultramafic complexes: metamorphic modifications. International Geology Review 38 (3), 245-267.

Takahashi, E., Uto, K., Schilling, J.G., 1987. Primary magma compositions and Mg/Fe ratios of their mantle residues along mid-Atlantic ridge 29N to 73N Technical Report, A9. Institute of Studies Earth's Interior, Okayama University Series, pp.1-14.

Uysal, I., Ersoy, E.Y., Dilek, Y., Kapsiotis, A., Sarıfakıoğlu, E., 2016. Multiple episodes of partial melting, depletion, metasomatism and enrichment processes recorded in the heterogeneous upper mantle sequence of the Neotethyan Eldivan ophiolite, Turkey. Lithos 246, 228-245.

Uysal, I., Yalçin Ersoy, E., Karsli, O., Dilek, Y., Burhan Sadiklar, M., Ottley, C.J., Tiepolo, M., Meisel, T., 2012. Coexistence of abyssal and ultra-depleted SSZ type mantle peridotites in a Neo-Tethyan Ophiolite in SW Turkey: Constraints from mineral composition, whole-rock geochemistry (major-trace-REE-PGE), and Re-Os isotope systematics. Lithos 132-133, 50-69.

Whitehouse, M.J., Stoeser, D., Stacey, J.S., 2001. The Knida Terrane — geochronological and Isotopic Evidence for Paleoproterozoic and Archean Crust in the Eastern Arabian Shield of Saudi Arabia. Gondwana Research 4, 200–202.

Workman, R.K., Hart, S.R., 2005. Major and trace element composition of the depleted MORB mantle (DMM). Earth and Planetary Science Letters 231(1-2), 53-72.

Zhou, M. F., Robinson, P. T., Malpas, J., 2005. REE and PGE Geochemical Constraints on the Formation of Dunites in the Luobusa Ophiolite, Southern Tibet. Journal of Petrology 46(3), 615–639.

Zhou, M.F., Robinson, P.T., Malpas, J., Li, Z., 1996. Podiform chromitites in the Luobusa ophiolite (southern Tibet): implications for melt-rock interaction and chromite segregation in the upper mantle. Journal of Petrology 37(1), 3-21.

Figure captions

Figure 1. Regional tectonic map of the Arabian Shield showing the distribution of ophiolite belts in Saudi Arabia (after Nehlig et al., 2002) and showing terrane ages from Kröner et al. (1991), Pallister et al. (1988), Whitehouse et al. (2001), Dilek and Ahmed 2003, Hargrove et al. (2006a,b). The location of the studied area (Fig. 2) is indicated.

Figure 2. Geological map of Bir Tuluhah area modified after Kattan (1983) and Habtoor et al. (2017).

Figure 3. Photomicrographs of the Bir Tuluhah ophiolite suite. (a) Chrysotile vein in serpentinized harzburgite; (b) mesh and bastite textures indicating replacement of olivine and orthopyroxene, respectively; (c) fresh relics of olivine; (d) a band of disseminated chromite in serpentinized harzburgite; (e) massive chromitite with minor serpentine along grain boundaries and cracks; and (f) sheared chromitite with schistose texture. All images in plane-polarized transmitted light except (a, c), which is cross-polarized transmitted light.

Figure 4. (a) NiO and Fo contents of olivine in the Bir Tuluhah serpentinized harzburgite and dunite compared to the mantle olivine array (Takahashi et al., 1987) and (b) Cr# vs. Mg# diagram for fresh chromian spinels (after Stern et al,. 2004); the field boundaries are from Dick and Bullen (1984), Bloomer et al. (1995) and Ohara et al. (2002).

Figure 5. (a) Cr# vs. TiO_2 diagram for spinels (fields after Dick and Bullen 1984; Jan and Windley, 1990) and (b) Al_2O_3 vs. Fe^{2+}/Fe^3 diagram for spinel; fields of spinel from SSZ and abyssal peridotites are from Kamenetsky et al. (2001).

Figure 6. Results of a quantitative thermodynamic model for precipitation of chromite by melt mixing. The figure shows the phase diagram at constant pressure (0.1 GPa) along a binary join (see Table 5) between the composition of the boninite liquid residual to dunite

formation (with 55.4 wt.% SiO_2, on the right side of the plot) and the composition of the primary aggregate fractional melt generated from the solidus up to an extraction pressure of 1.0 GPa (with 46.6 wt.% SiO_2, off-scale to the left). All the oxides vary together along this join, but for convenience the compositions are indexed by wt. % SiO_2. Phase relations are computed with the MELTS model (Ghiorso and Sack, 1995). The heavy green line shows the saturation temperature where olivine begins to crystallize; note that olivine is the liquidus phase at both edges of the diagram. The heavy black line shows the saturation temperature where Cr-spinel begins to crystallize; note that Cr-spinel is the liquidus phase in the central region of the diagram. The light blue lines show contours of mass fraction spinel in the equilibrium assemblage. The maximum mass of Cr-spinel that can be crystallized before olivine begins to crystallize is 0.012 wt. %, or 1 g of spinel from 8.3 kg of melt.

Table 1 . Representative microprobe analyses of fresh olivine in the serpentinized harzbergite and dunite of Bir Tuluhah ophiolite.

Rock type	Harzbergite										Dunite									
Sample No.	TH4					TH17					TD 9					TD22				
Spot No.	Ol#1	Ol#3	Ol#5	Ol#8	Ol#11	Ol#1	Ol#4	Ol#7	Ol#10		OL #1	OL #2	OL #4	OL #8	OL #9	OL #10	OL #11	OL #14	OL #16	OL #18
SiO2	40.81	41.12	40.95	40.97	41.15	40.87	41.07	41.18	40.89	40.84	41.05	40.91	40.88	39.89	41.01	41.48	40.93	41.17	41.02	40.87
TiO2	0.004	0.003	0.004	0.005	0.003	0.004	0.005	0	0.008	0.003	0.002	0.007	0.005	0.006	0.008	0.004	0.009	0.008	0.013	0.007
Al2O3	0.002	0.003	0.001	0.004	0.011	0.006	0.004	0.003	0.006	0.006	0.008	0.005	0.012	0.002	0.006	0.007	0.003	0.007	0.003	0.004
Cr2O3	0.013	0.028	0.012	0.012	0.022	0.023	0.014	0.019	0.017	0.018	0.008	0.002	0.025	0.015	0.018	0.004	0.013	0.011	0.024	0.007
FeO	8.816	9.585	8.982	8.592	8.896	9.235	8.886	9.437	9.005	8.767	7.296	7.48	7.54	7.543	7.921	7.073	7.43	7.665	7.577	7.473
MnO	0.121	0.123	0.139	0.148	0.131	0.135	0.134	0.114	0.129	0.123	0.157	0.147	0.14	0.126	0.137	0.13	0.135	0.131	0.123	0.119
MgO	49.66	49.55	49.53	49.28	49.25	48.72	49.64	49.55	48.97	49.65	50.88	51.06	50.99	51.35	50.41	51.09	51.1	50.67	50.75	50.99
CaO	0.042	0.032	0.029	0.035	0.03	0.035	0.026	0.032	0.027	0.021	0.027	0.026	0.039	0.033	0.034	0.023	0.029	0.023	0.037	0.031
NiO	0.445	0.421	0.427	0.395	0.446	0.408	0.397	0.436	0.421	0.367	0.432	0.503	0.483	0.441	0.484	0.465	0.488	0.48	0.519	0.519
Total	99.918	###	99.842	99.445	99.935	99.441	###	###	99.516	99.3	99.92	100.2	99.98	99.4	100	100.3	100.2	100.2	100.1	100
Si	0.998	0.999	1.002	1.005	1.006	1.006	1.001	1.001	1.004	0.999	0.998	0.993	0.994	0.978	0.998	1.002	0.993	0.999	0.997	0.994
Ti	0.000	0.000	0.000	0.000	0.000	0.000	0.000	0.000	0.000	0.000	0.000	0.000	0.000	0.000	0.000	0.000	0.000	0.000	0.000	0.000
Al	0.000	0.000	0.000	0.000	0.000	0.000	0.000	0.000	0.000	0.000	0.000	0.000	0.000	0.000	0.000	0.000	0.000	0.000	0.000	0.000
Cr	0.000	0.001	0.000	0.000	0.000	0.000	0.000	0.000	0.000	0.000	0.000	0.000	0.000	0.000	0.000	0.001	0.000	0.000	0.000	0.000
Fe(ii)	0.180	0.195	0.184	0.176	0.182	0.190	0.181	0.192	0.186	0.179	0.148	0.152	0.150	0.155	0.161	0.143	0.151	0.155	0.154	0.152
Mn	0.003	0.003	0.003	0.003	0.003	0.003	0.003	0.002	0.003	0.003	0.003	0.003	0.003	0.003	0.003	0.003	0.003	0.003	0.003	0.002
Mg	1.811	1.795	1.799	1.808	1.797	1.787	1.805	1.795	1.793	1.811	1.843	1.848	1.848	1.877	1.829	1.840	1.849	1.833	1.838	1.848
Ni	0.009	0.008	0.008	0.008	0.009	0.008	0.008	0.009	0.008	0.007	0.009	0.010	0.009	0.009	0.009	0.009	0.010	0.009	0.010	0.010
Ca	0.001	0.001	0.001	0.001	0.001	0.001	0.001	0.001	0.001	0.001	0.001	0.001	0.001	0.001	0.001	0.001	0.001	0.001	0.001	0.001
Fo	0.91	0.90	0.91	0.91	0.91	0.90	0.91	0.90	0.91	0.91	0.93	0.92	0.92	0.92	0.92	0.93	0.92	0.92	0.92	0.92

Table 2. Representative electron microprobe analyses of fresh Cr-spinel in the serpentinized harzburgite and dunite of Bir Tuluhah ophiolite.

Rock type	Harzburgite										Dunite									
Sample No.	TH4					TH17					TD9					TD22				
Spot No.	Sp-1	Sp-2	Sp-4	Sp-6	Sp-14	Sp-1	Sp-3	Sp-7	Sp-9	Sp-12	Sp-1	Sp-4	Sp-5	Sp-10	Sp-12	Sp-1	Sp-5	Sp-6	Sp-12	Sp-13
SiO2	0.028	0.032	0.044	0.523	0.02	0.025	0.12	0.037	0.59	0.024	0.028	0.018	0.039	0.2121	0.1818	0.0117	0.0017	0.0888	0.05	0.195
TiO2	0.079	0.067	0.059	0.076	0.094	0.106	0.093	0.083	0.125	0.107	0.061	0.057	0.066	0.04	0.015	0.021	0.062	0.038	0.037	0.047
Al2O3	20.12	20.046	18.716	19.33	22.615	22.675	22.184	22.48	23.936	23.746	17.227	15.27	16.037	15.898	16.233	16.037	17.7	14.751	16.611	16.241
FeO	15.895	16.065	16.73	15.94	16.816	16.26	15.639	15.642	13.671	15.746	14.241	14.696	14.164	14.157	15.905	15.842	12.362	10.466	13.81	11.993
MgO	12.912	12.692	12.126	13.482	11.06	10.614	12.516	10.537	11.74	10.81	13.883	14.117	14.185	13.634	12.645	12.579	13.211	15.859	14.251	13.581
CaO	0	0	0	0.001	0.006	0.001	0.004	0.001	0.008	0.006	0	0	0.004	0.03	0	0	0.01	0.05	0.09	0.026
Na2O	0.003	0.001	0.003	0.005	0	0	0	0	0.049	0.001	0	0.011	0.004	0.017	0.005	0.009	0.008	0.002	0.04	0.01
K2O	0.003	0.003	0	0.003	0.001	0.002	0	0	0.022	0	0	0	0.001	0.001	0	0	0	0.001	0	0
Cr2O3	49.491	49.523	50.823	49.202	48.996	49.062	47.794	49.879	48.41	48.546	51.794	54.39	53.688	53.99	53.291	53.479	54.653	57.211	53.503	55.585
MnO	0.333	0.335	0.353	0.346	0.318	0.305	0.327	0.317	0.3	0.297	0.367	0.365	0.352	0.376	0.366	0.36	0.348	0.359	0.374	0.343
NiO	0.174	0.145	0.096	0.064	0.08	0.06	0.075	0.05	0.072	0.091	0.11	0.131	0.123	0.09	0.132	0.106	0.03	0.059	0.075	0.051
Total	99.038	98.909	98.95	98.972	100.006	99.11	98.752	99.037	98.93	99.376	98.711	99.055	98.663	98.628	98.604	98.45	98.401	98.884	98.724	98.072
Ti	0.002	0.002	0.001	0.002	0.002	0.003	0.002	0.002	0.003	0.003	0.001	0.000	0.000	0.001	0.000	0.000	0.003	0.003	0.001	0.003
Al	0.742	0.741	0.699	0.716	0.830	0.841	0.816	0.836	0.883	0.874	0.641	0.570	0.598	0.596	0.612	0.606	0.662	0.546	0.618	0.612
Cr	1.225	1.229	1.272	1.222	1.216	1.221	1.180	1.244	1.198	1.199	1.317	1.361	1.344	1.359	1.347	1.356	1.372	1.421	1.335	1.406
Fe3+	0.030	0.026	0.026	0.059	0.04	0.067	0.001	0.084	0.087	0.078	0.040	0.068	0.057	0.043	0.041	0.038	0.039	0.026	0.046	0.024
Fe2+	0.386	0.395	0.417	0.360	0.478	0.495	0.409	0.497	0.445	0.489	0.336	0.321	0.318	0.342	0.385	0.386	0.367	0.249	0.319	0.345
Mn	0.009	0.009	0.009	0.009	0.008	0.008	0.009	0.008	0.008	0.008	0.010	0.010	0.009	0.010	0.010	0.010	0.009	0.010	0.010	0.009
Ni	0.004	0.004	0.002	0.002	0.002	0.002	0.002	0.001	0.002	0.002	0.003	0.003	0.003	0.002	0.003	0.003	0.001	0.001	0.002	0.001
Mg	0.602	0.594	0.572	0.631	0.513	0.498	0.583	0.496	0.548	0.503	0.653	0.666	0.670	0.647	0.603	0.601	0.625	0.743	0.670	0.648
Cr#	0.62	0.62	0.65	0.63	0.59	0.59	0.59	0.60	0.58	0.58	0.67	0.71	0.69	0.70	0.69	0.69	0.67	0.72	0.68	0.70
Mg#	0.59	0.58	0.56	0.60	0.54	0.54	0.59	0.55	0.60	0.55	0.63	0.63	0.64	0.63	0.59	0.59	0.66	0.73	0.65	0.67
Fe^{3+}#	0.01	0.01	0.01	0.03	-0.02	-0.03	0.00	-0.04	-0.04	-0.04	0.02	0.03	0.03	0.02	0.02	0.02	-0.02	0.01	0.02	-0.01

Table 3. Representative electron microprobe analyses of fresh Cr-spinel in the chromitite lenses of Bir Tuluhah ophiolite.

Sample No.	TCR-2							TCR-9						TCR-16						
Spot No.	Sp-1	Sp-2	Sp-4	Sp-8	Sp-9	Sp-11	Sp-12	Sp-1	Sp-2	Sp-5	Sp-9	Sp-10	Sp-17	Sp-1	Sp-6	Sp-9	Sp-11	Sp-15	Sp-20	Sp-21
SiO2	0.019	1.313	0.01	0.297	0.07	0.667	0.047	0.038	0.02	0.01	0.14	0.302	0.098	0.042	0.025	0.01	0.014	0.054	0.133	0.057
TiO2	0.028	0.106	0.101	0.102	0.098	0.087	0.025	0.101	0.104	0.123	0.085	0.055	0.078	0.126	0.209	0.112	0.111	0.137	0.067	0.123
Al2O3	13.09	11.445	15.586	12.144	9.587	8.782	11.827	12.143	12.318	12.259	11.543	11.013	11.734	11.[illegible]	10.755	10.858	10.63	11.032	9.762	11.192
FeO	12.87	13.534	11.067	12.082	13.177	13.194	13.101	16.516	16.482	16.424	14.578	16.062	14.[illegible]	15.[illegible]4	13.295	13.507	13.449	14.098	14.059	14.639
MgO	15.476	16.391	14.99	16.921	15.323	16.623	15.235	15.143	15.242	15.141	16.549	14.94	16.663	15.572	15.246	15.525	15.628	15.471	15.25	15.477
Cr2O3	56.252	55.275	57.561	57.52	59.59	59.161	57.832	53.743	53.621	53.774	55.16[illegible]	57.[illegible]	54.759	54.826	58.521	57.579	57.896	57.328	58.981	56.42
MnO	0.413	0.545	0.422	0.51	0.573	0.581	0.443	0.555	0.558	0.56	0.541	0.507	0.547	0.554	0.521	0.529	0.512	0.515	0.468	0.563
NiO	0.092	0.032	0.019	0.299	0.047	0.053	0.068	0.079	0.08	0.081	0.072	0.069	0.073	0.08	0.08	0.096	0.075	0.06	0.057	0.075
Total	98.24	98.641	99.756	99.875	98.465	99.148	98.578	98.831	98.[illegible]3	98.368	98.669	98.718	98.505	98.366	98.652	98.216	98.315	98.695	98.777	98.546
Ti	0.001	0.004	0.002	0.005	0.002	0.002	0.001	0.005	0.005	0.005	0.004	0.004	0.004	0.005	0.005	0.004	0.005	0.005	0.004	0.004
Al	0.492	0.433	0.574	0.448	0.365	0.332	0.[illegible]16	0.[illegible]37	0.463	0.461	0.431	0.423	0.438	0.437	0.407	0.411	0.402	0.416	0.370	0.422
Cr	1.416	1.402	1.423	1.422	1.522	1.[illegible]09	1.463	1.358	1.351	1.358	1.381	1.490	1.370	1.384	1.485	1.462	1.469	1.449	1.501	1.427
Fe3+	0.090	0.159	-0.002	0.121	0.108	0.[illegible]1	0.090	0.175	0.176	0.172	0.179	0.079	0.183	0.169	0.098	0.119	0.119	0.125	0.120	0.143
Fe2+	0.252	0.204	0.292	0.[illegible]93	0.[illegible]46	0.[illegible]90	0.260	0.266	0.263	0.267	0.207	0.359	0.202	0.246	0.259	0.244	0.241	0.252	0.258	0.249
Mn	0.011	0.015	0.011	0.014	0.[illegible]3	0.016	0.012	0.015	0.015	0.015	0.015	0.014	0.015	0.015	0.014	0.014	0.014	0.014	0.013	0.015
Ni	0.002	0.001	0.000	0.008	0.001	0.001	0.002	0.002	0.002	0.002	0.002	0.002	0.002	0.002	0.002	0.002	0.002	0.002	0.001	0.002
Mg	0.735	0.784	0.699	0.789	0.738	0.795	0.727	0.721	0.724	0.721	0.781	0.629	0.786	0.741	0.730	0.743	0.748	0.738	0.732	0.738
Cr#	0.74	0.76	0.71	0.76	0.81	0.82	0.77	0.75	0.74	0.75	0.76	0.78	0.76	0.76	0.79	0.78	0.79	0.78	0.80	0.77
Mg#	0.68	0.68	0.71	0.71	0.67	0.69	0.67	0.62	0.62	0.62	0.67	0.59	0.67	0.64	0.67	0.67	0.67	0.66	0.66	0.65

Table 4. Inclusions of olivine in the chromitite of Bir Tuluhah.

Mineral	Olivine					
Sample No.	TCR-2			TCR-16		
Spot No.	OL#1	OL#2	OL#2	OL#1	OL#2	OL#3
SiO2	40.645	40.454	40.874	40.76	40.78	40.728
TiO2	0.005	0.007	0.006	0.003	0.008	0.005
Al2O3	0.015	0.015	0.029	0.023	0.018	0.021
Cr2O3	0.223	0.159	0.162	0.121	0.164	0.265
FeO	5.544	4.667	5.12	4.887	5.12	5.409
MnO	0.054	0.077	0.101	0.072	0.091	0.107
MgO	53.009	53.768	53.23	53.433	53.146	52.961
NiO	0.547	0.851	0.586	0.68	0.728	0.604
CaO	0.034	0.032	0.037	0.029	0.051	0.028
Total	100.076	100.03	100.145	100.008	100.106	100.128
Si	0.980	0.975	0.984	0.981	0.983	0.982
Ti	0.000	0.000	0.000	0.000	0.000	0.000
Al	0.000	0.000	0.001	0.001	0.001	0.001
Cr	0.004	0.003	0.003	0.002	0.003	0.005
Fe(ii)	0.112	0.094	0.103	0.098	0.103	0.109
Mn	0.004	0.004	0.003	0.004	0.002	0.004
Mg	1.906	1.931	1.910	1.917	1.909	1.903
Ni	0.011	0.016	0.011	0.013	0.014	0.012
Ca	0.001	0.001	0.001	0.001	0.001	0.001
Fo	0.94	0.95	0.95	0.95	0.95	0.95

Table 5. Compositional end-members of MELTS-based thermodynamic mixing model

	Pressure (GPa)	SiO_2	TiO_2	Al_2O_3	Fe_2O_3	Cr_2O_3	FeO	MnO	MgO	NiO	CaO	Na_2O	H_2O
Mantle source	3.3	44.71	0.13	3.98	0.191	0.57	8.008	0.13	38.773	0.24	3.17	0.28	0.015
Aggregate primary liquid	1.0	46.580	0.782	16.015	0.134	0.045	6.826	0.167	13.357	0.046	14.261	1.696	0.091
Reacted boninitic liquid	0.1	55.415	0.307	12.498	0.434	0.368	5.518	0.134	13.675	0.052	10.049	0.127	1.424

Highlights

- Serpentinized ultramafics of Bir Tuluhah have relict primary mantle minerals
- Fresh relics of olivine have high Fo and NiO contents, similar to mantle olivines
- Extensive melt depletion of ultramafic protoliths suggests a fore-arc setting
- Chromitites and host ultramafic rocks are crystallized from boninitic magma
- Chromitites represent the residues of melt-rock interaction

Graphical abstract

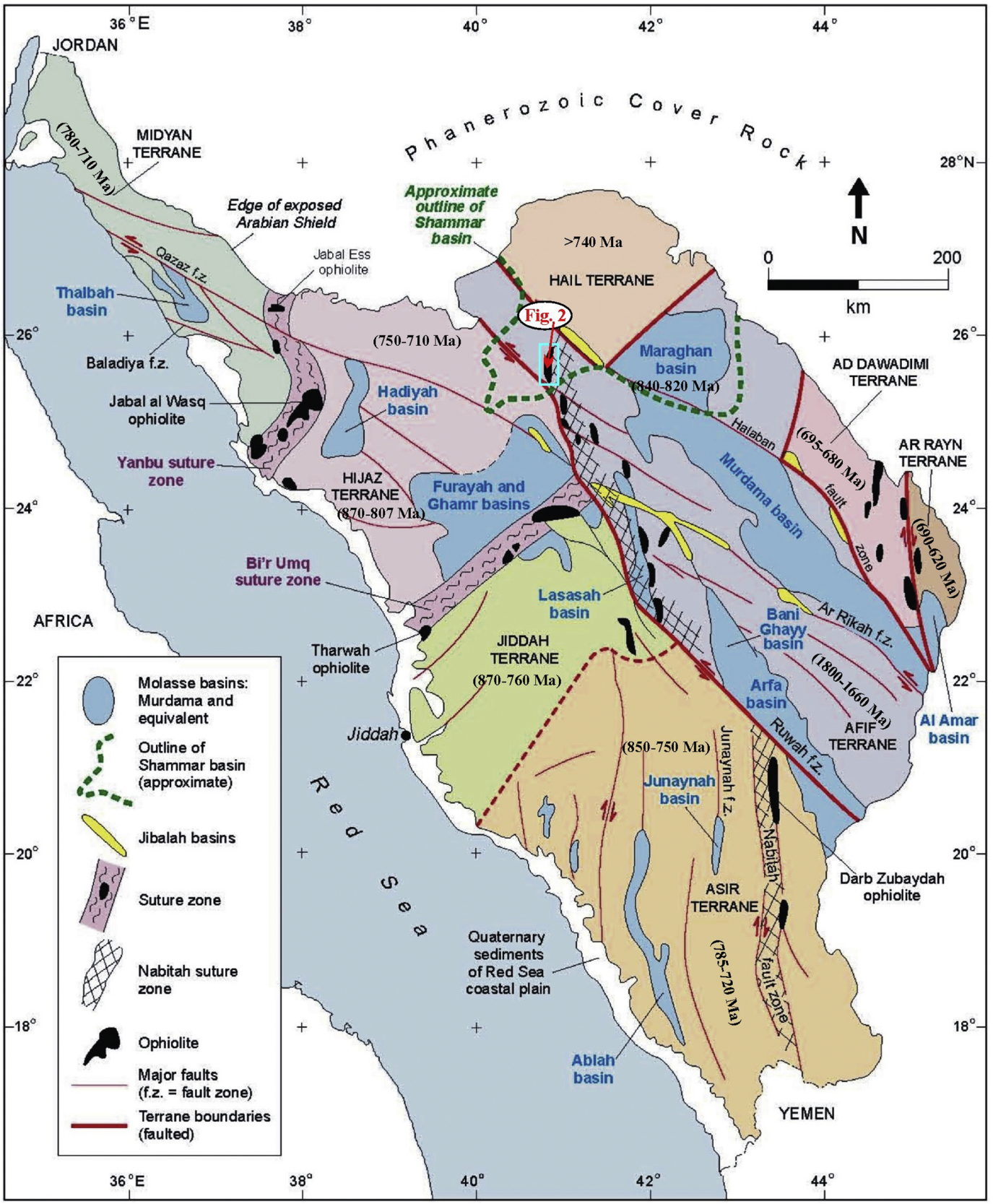
36°E
38°
40°
42°
44°
28°N
26°
24°
22°
20°
18°
JORDAN
MIDYAN TERRANE
(780-710 Ma)
Phanerozoic Cover Rock
Edge of exposed Arabian Shield
Approximate outline of Shammar basin
>740 Ma
HAIL TERRANE
Jabal Ess ophiolite
Qazaz f.z.
Thalbah basin
Baladiya f.z.
Fig. 2
(750-710 Ma)
Maraghan basin
(840-820 Ma)
AD DAWADIMI TERRANE
Jabal al Wasq ophiolite
Hadiyah basin
Halaban
(695-680 Ma) fault zone
AR RAYN TERRANE
Yanbu suture zone
HIJAZ TERRANE
(870-807 Ma)
Furayah and Ghamr basins
Murdama basin
(690-620 Ma)
Bi'r Umq suture zone
Lasasah basin
Ar Rikah f.z.
Bani Ghayy basin
AFRICA
Tharwah ophiolite
JIDDAH TERRANE
(870-760 Ma)
(1800-1660 Ma)
Arfa basin
Al Amar basin
Jiddah
(850-750 Ma)
Junaynah f.z.
Ruwah f.z.
AFIF TERRANE
Junaynah basin
Nabitah f.z.
Darb Zubaydah ophiolite
ASIR TERRANE
(785-720 Ma)
fault zone
Red Sea
Quaternary sediments of Red Sea coastal plain
Ablah basin
YEMEN
N
0
200
km
Molasse basins: Murdama and equivalent
Outline of Shammar basin (approximate)
Jibalah basins
Suture zone
Nabitah suture zone
Ophiolite
Major faults (f.z. = fault zone)
Terrane boundaries (faulted)

Figure 1

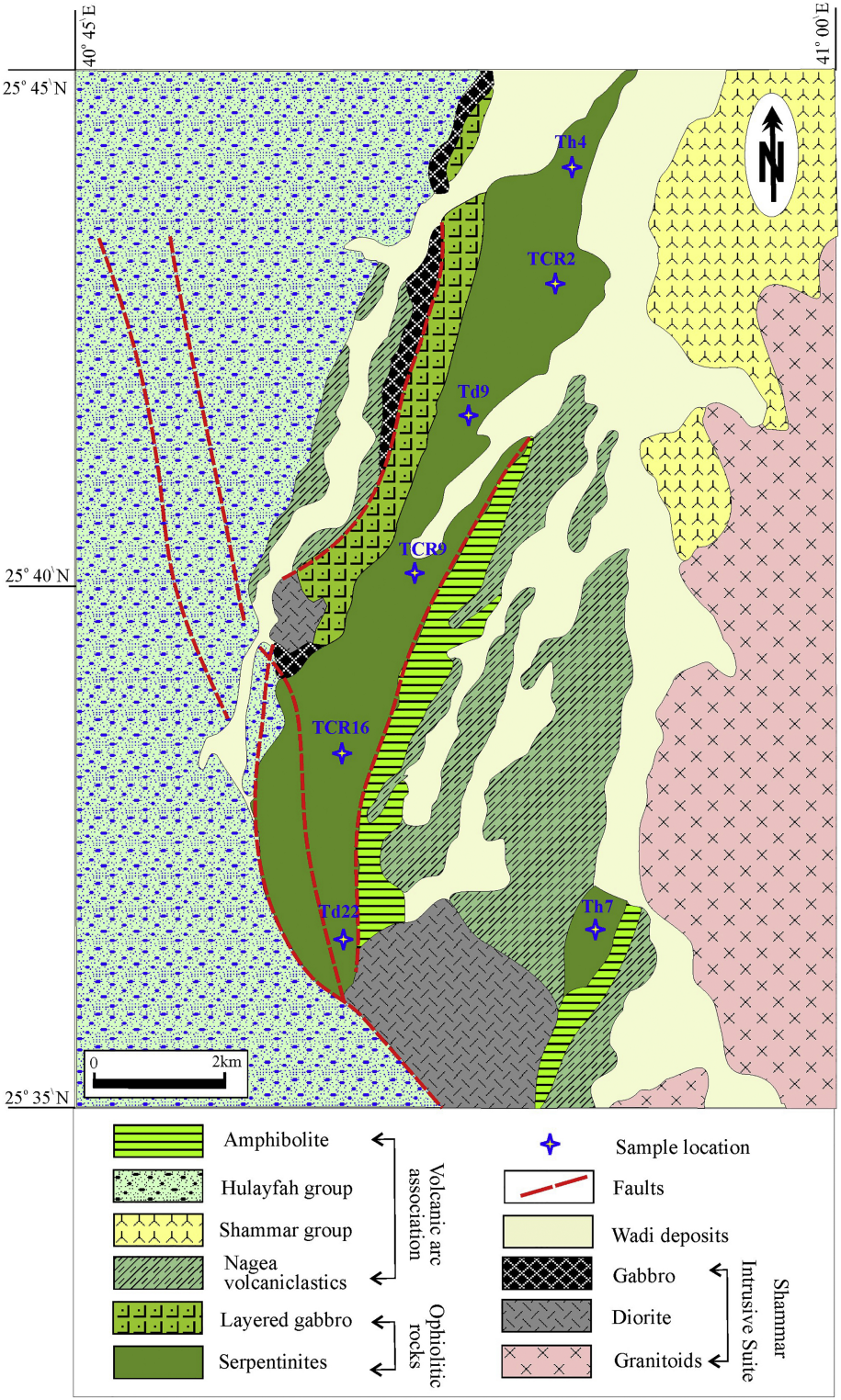
40° 45' E
41° 00' E
25° 45' N
25° 40' N
25° 35' N
Th4
TCR2
Td9
TCR9
TCR16
Td22
Th7
N
0
2km
Amphibolite
Hulayfah group
Shammar group
Nagea volcaniclastics
Volcanic arc association
Layered gabbro
Serpentinites
Ophiolitic rocks
Sample location
Faults
Wadi deposits
Gabbro
Diorite
Granitoids
Shammar Intrusive Suite

Figure 2

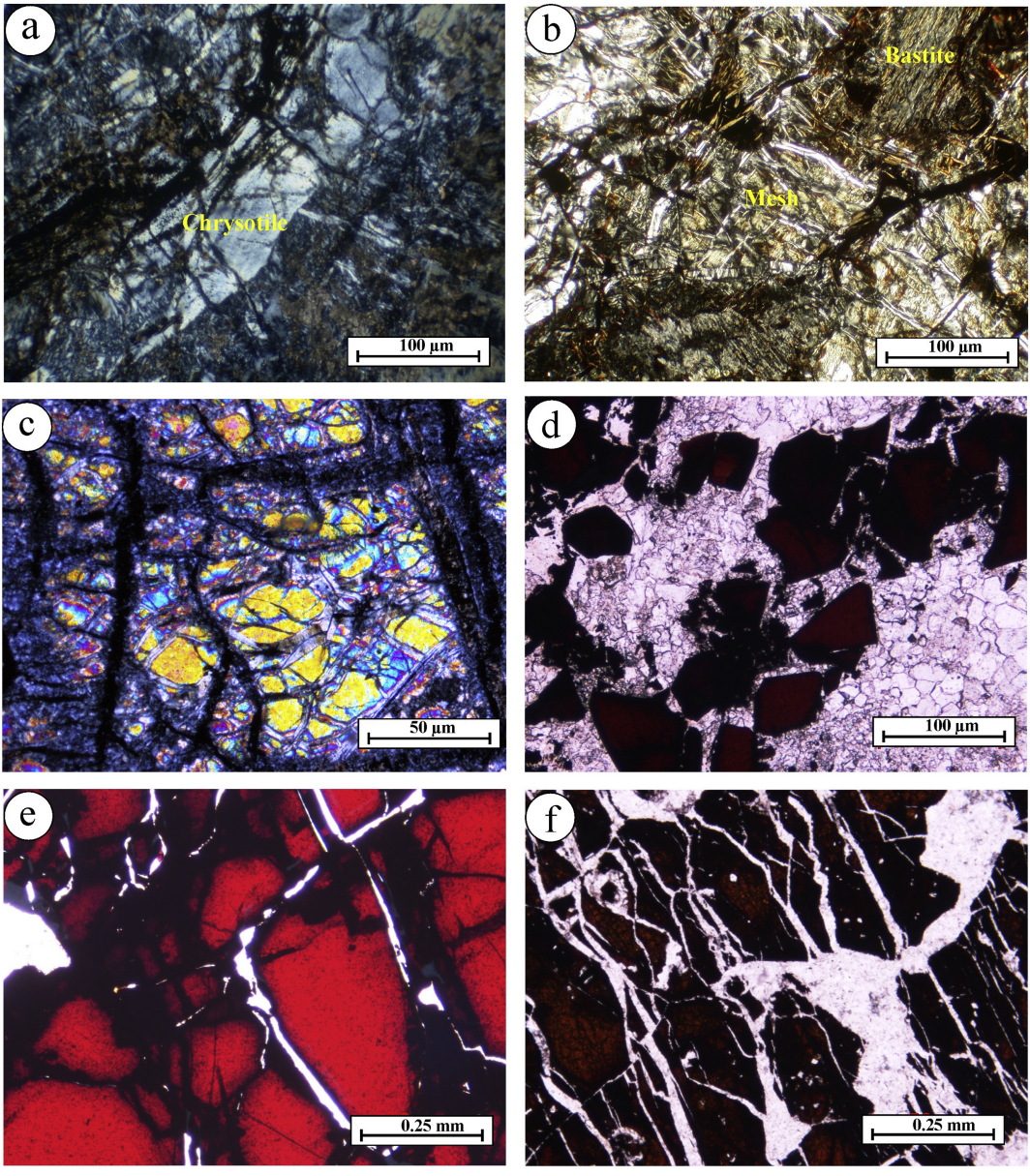
a
Chrysotile
100 µm
b
Bastite
Mesh
100 µm
c
50 µm
d
100 µm
e
0.25 mm
f
0.25 mm

Figure 3

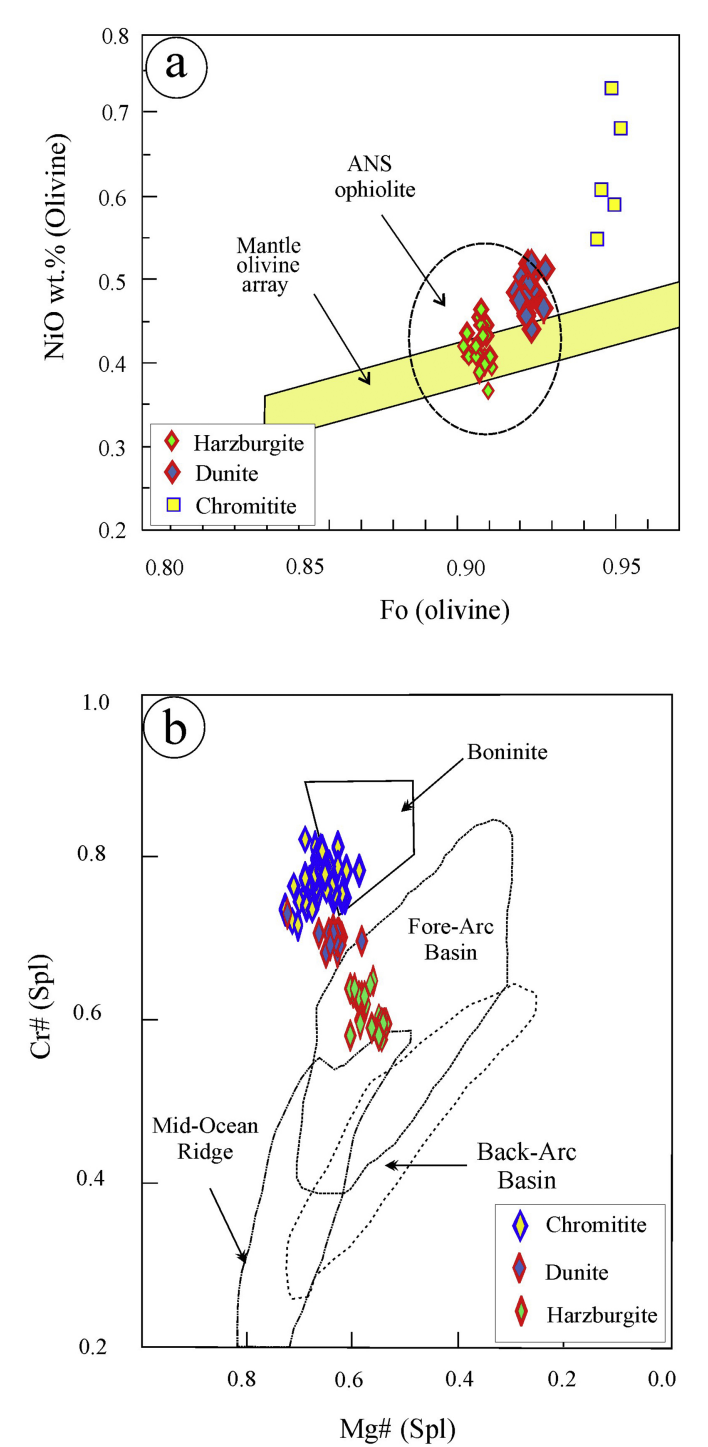
a
NiO wt.% (Olivine)
0.8
0.7
0.6
0.5
0.4
0.3
0.2
ANS
ophiolite
Mantle
olivine
array
Harzburgite
Dunite
Chromitite
0.80
0.85
0.90
0.95
Fo (olivine)
b
Cr# (Spl)
1.0
0.8
0.6
0.4
0.2
Boninite
Fore-Arc
Basin
Mid-Ocean
Ridge
Back-Arc
Basin
Chromitite
Dunite
Harzburgite
0.8
0.6
0.4
0.2
0.0
Mg# (Spl)

Figure 4

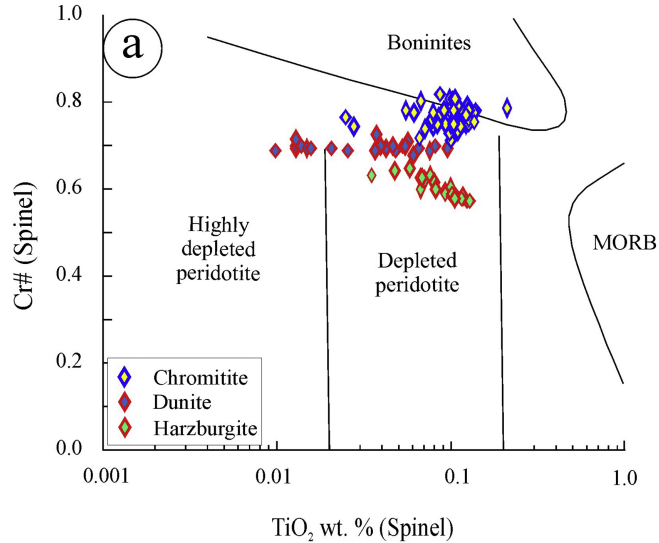
a
Boninites
Highly depleted peridotite
Depleted peridotite
MORB
Chromitite
Dunite
Harzburgite
Cr# (Spinel)
TiO2 wt. % (Spinel)
1.0
0.8
0.6
0.4
0.2
0.0
0.001
0.01
0.1
1.0

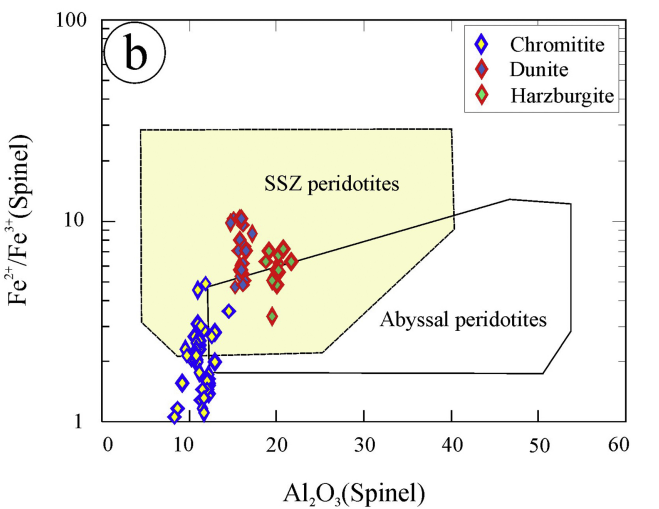
b
Chromitite
Dunite
Harzburgite
SSZ peridotites
Abyssal peridotites
Fe2+/Fe3+(Spinel)
Al2O3(Spinel)
100
10
1
0
10
20
30
40
50
60

Figure 5

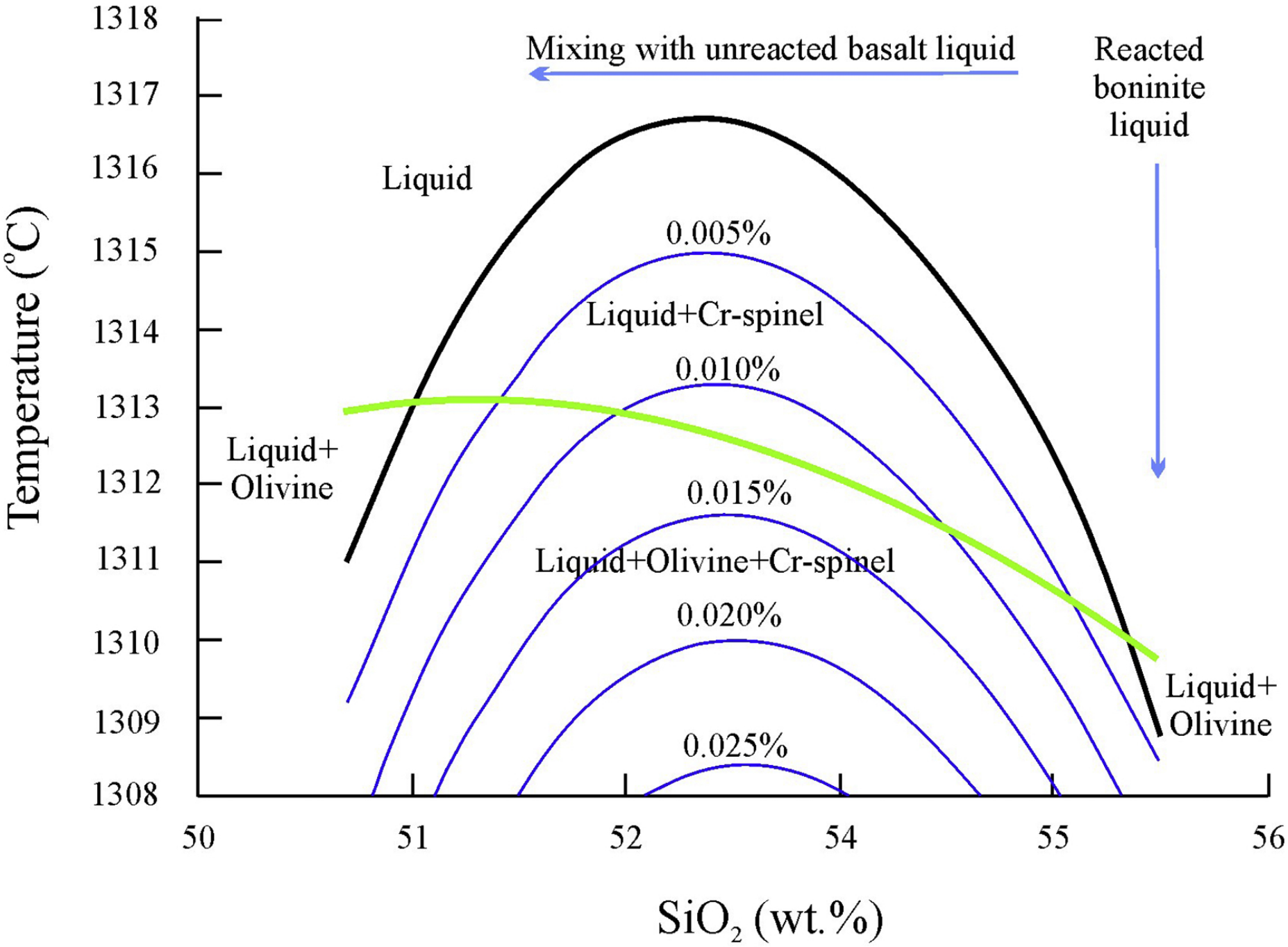
Mixing with unreacted basalt liquid
Reacted boninite liquid
Liquid
0.005%
Liquid+Cr-spinel
0.010%
Liquid+ Olivine
0.015%
Liquid+Olivine+Cr-spinel
0.020%
Liquid+ Olivine
0.025%
Temperature (°C)
1318
1317
1316
1315
1314
1313
1312
1311
1310
1309
1308
50
51
52
54
55
56
SiO2 (wt.%)

Figure 6